



Statistical Analysis of Supernova Remnants in the Large Magellanic Cloud

Luke M. Bozzetto¹, Miroslav D. Filipović¹, Branislav Vukotić², Marko Z. Pavlović³, Dejan Urošević^{3,4}, Patrick J. Kavanagh⁵,
Bojan Arbutina³, Pierre Maggi⁶, Manami Sasaki⁷, Frank Haberl⁸, Evan J. Crawford¹,
Quentin Roper¹, Kevin Grieve¹, and S. D. Points⁹

¹ Western Sydney University, Locked Bag 1797, Penrith South DC, NSW 1797, Australia; m.filipovic@westernsydney.edu.au

² Astronomical Observatory, Volgina 7, 11060 Belgrade 38, Serbia

³ Department of Astronomy, Faculty of Mathematics, University of Belgrade, Studentski trg 16, 11000 Belgrade, Serbia

⁴ Isaac Newton Institute of Chile, Yugoslavia Branch

⁵ School of Cosmic Physics, Dublin Institute for Advanced Studies, 31 Fitzwilliam Place, Dublin 2, Ireland

⁶ Laboratoire AIM, IRFU/Service d'Astrophysique—CEA/DRF—CNRS—Université Paris Diderot, Bat. 709, CEA-Saclay, F-91191 Gif-sur-Yvette Cedex, France

⁷ Dr. Karl Remeis-Sternwarte, Erlangen Centre for Astroparticle Physics, Friedrich-Alexander-Universität Erlangen-Nürnberg,
Sternwartstraße 7, D-96049 Bamberg, Germany

⁸ Max-Planck-Institut für extraterrestrische Physik, Giessenbachstraße, D-85748 Garching, Germany

⁹ Cerro Tololo Inter-American Observatory, Casilla 603, La Serena, Chile

Received 2016 July 3; revised 2017 February 25; accepted 2017 March 3; published 2017 May 3

Abstract

We construct the most complete sample of supernova remnants (SNRs) in any galaxy—the Large Magellanic Cloud (LMC) SNR sample. We study their various properties such as spectral index (α), size, and surface brightness. We suggest an association between the spatial distribution and environment density of LMC SNRs, and their tendency to be located around supergiant shells. We find evidence that the 16 known type Ia LMC SNRs are expanding in a lower density environment compared to the Core-Collapse (CC) type. The mean diameter of our entire population (74) is 41 pc, which is comparable to nearby galaxies. We did not find any correlation between the type of SN explosion, ovality, or age. The $N(<D)$ relationship with slope $a = 0.96$ implies that the randomized diameters are readily mimicking such an exponent. The rate of SNe occurring in the LMC is estimated to be ~ 1 per 200 yr. The mean α of the entire LMC SNR population is -0.52 , which is typical of most SNRs. However, our estimates show a clear flattening of the synchrotron α as the remnants age. As predicted, the CC SNRs in our sample are significantly brighter radio emitters than type Ia remnants. We also estimate the Σ – D relation for the LMC to have a slope ~ 3.8 , which is comparable with other nearby galaxies. We also find the residency time of electrons in the galaxy (4.0–14.3 Myr), implying that SNRs should be the dominant mechanism for the production and acceleration of CRs.

Key words: acceleration of particles – ISM: supernova remnants – Local Group – radio continuum: ISM

1. Introduction

Observational facts that we have gathered over the past decades, together with statistical analysis of the Large Magellanic Cloud (LMC) Supernova Remnant (SNR) population, are essential for our understanding of the processes in these violent celestial objects. The LMC is a galaxy that provides one of the rare opportunities to gather information on a population of SNRs that is close enough to be resolved spatially. Moderate-to-high resolution images ($<1'$) are available at all wavelengths, allowing for a more stringent classification of this class of objects, yielding a more credible population. Apart from the Small Magellanic Cloud (SMC), the only other galaxy for which such resolution is attainable is our own, the Milky Way (MW), where the highest resolution observations are possible. However, the MW sample is not without its own drawbacks. It is affected by the Malmquist bias,¹⁰ making the sample somewhat incomplete, as well as suffering from distance uncertainties and the absence of uniform coverage. Such challenges are not as pronounced when observing SNRs in the LMC, and we can assume that the intrinsic LMC objects are located at approximately the same distance. We acknowledge that the inclination of the LMC toward the line of sight (Subramanian & Subramanian 2010)

may introduce up to a $\sim 10\%$ error in distance when the SNR is positioned closer to the southern end, compared with objects at the northern end of the LMC.

The first SNR candidates in the LMC were presented by Mathewson & Healey (1964), and later confirmed by Westerlund & Mathewson (1966) through follow-up radio and optical observations. These three remnants (N49, N63A, and N132D) were, in fact, the first extragalactic SNRs ever discovered. Since then, there have been a considerable number of additions to that population, with notable samples from Mathewson & Clarke (1973), Milne et al. (1980), Long et al. (1981), Mathewson et al. (1983, 1984, 1985), and Mills et al. (1984). Numerous surveys have also been undertaken in various electromagnetic (EM) spectral bands. For example, Chu & Kennicutt (1988) looked into the population and environments of SNRs in the LMC. In the radio continuum, Filipović et al. (1998) carried out a study of the Magellanic Clouds (MCs). Haberl & Pietsch (1999, hereafter HP99) compiled an X-ray catalog of LMC sources, adding numerous SNR candidates to the population. Williams et al. (1999) produced an X-ray atlas of LMC SNRs, while Sasaki et al. (2000) compiled a *ROSAT* HRI catalog of X-ray sources in the LMC region. Blair et al. (2006) and Lakićević et al. (2015) surveyed SNRs in the MCs at far-UV wavelengths. Seok et al. (2013) presented a survey of infrared SNRs in the LMC. Most recently, Maggi et al. (2016) compiled the LMC SNR population seen with *XMM-Newton*.

¹⁰ The distance-dependent volume selection effect: brighter objects are favored in flux density-limited surveys.

A well-established (predominantly) non-thermal continuum emission is one of the distinguishing characteristics of SNRs at radio frequencies. The majority of SNRs have a radio spectral index of $\alpha \sim -0.5$ (defined as $S \propto \nu^\alpha$), although there is a large scatter because of the wide variety of SNRs and different environments and stages of evolution (Filipovic et al. 1998; Filipović & Bozzetto 2016). On one hand, younger and very old remnants can have a steeper spectral index of $\alpha \sim -0.8$, while mid-to-older aged remnants tend to have radio spectra with $\alpha \sim -0.5$. SNRs that harbour a Pulsar Wind Nebula (PWN) exhibit flatter radio spectra with $\alpha \sim -0.1$. As one of the most energetic class of sources in the universe, SN/SNRs greatly impact the structure, physical properties, and evolution of the interstellar medium (ISM) of the host galaxy. Conversely, the interstellar environments in which SNRs reside will heavily affect the remnants' evolution.

A complete sample of SNRs in any galaxy provides the opportunity to study the global properties of SNRs, in addition to carrying out a detailed analysis on the subclasses (e.g., sorted by X-ray and radio morphology or by progenitor SN type). Toward this goal, we have been identifying new LMC SNRs using combined optical, radio, IR, and X-ray observations. Apart from the above-mentioned LMC SNR survey papers, there are a number of studies focusing on particular LMC SNRs. Some recent studies include: Bojičić et al. (2007), Cajko et al. (2009), Crawford et al. (2008, 2010, 2014), Bozzetto et al. (2010, 2012a, 2012b, 2012c, 2012d, 2013, 2014a, 2014b, 2015), Brantseg et al. (2014), Grondin et al. (2012), de Horta et al. (2012, 2014), Kavanagh et al. (2013, 2015a, 2015b, 2015c, 2016), Bozzetto & Filipović (2014), Warth et al. (2014), Maggi et al. (2014), and Reid et al. (2015).

These major contributions, coupled with various additional studies, led to the discovery of 59 confirmed and an additional 15 candidate SNRs. Therefore, this is the first opportunity to perform a complete statistical study on a type of object that is crucial in galaxy evolution in one of the best laboratories available—the LMC. Here, we report on a radio-continuum study of the most up-to-date sample of the LMC SNRs and SNR candidates, consisting of 74 of these objects.

2. Observations

Common analysis methodologies were undertaken and shown for all remnants, such as emission images from across the EM spectrum including radio-continuum 36 cm (*MOST*; Mills & Turtle 1984), 20 cm (Hughes et al. 2007), and 6 cm (Dickel et al. 2010); infrared 24, 70, and 160 μm (SAGE; Meixner et al. 2006); optical (Magellanic Cloud Emission Line Survey, MCELS; Smith et al. 2000); and X-ray (LMC *XMM-Newton* Large Project; Haberl 2014 Maggi et al. 2016). The aforementioned radio-continuum mosaic images were also the default images used for flux density measurements at these wavelengths. Our own spectroscopic surveys of the MCs (Filipović et al. 2005; Payne et al. 2007, 2008) and their SNR samples were mainly taken with the SAAO 1.9 m and MSSSO 2.3 m telescopes.

3. Source List

The number of confirmed SNRs in the LMC is currently at 59 (as shown in Maggi et al. 2016; see also Table 1). In this paper, we used the same sample with the addition of a further 15 candidates, of which 7 are presented here for the

first time (Table 2). These seven new SNR candidates are MCSNR J0447-6919, MCSNR J0456-6950, MCSNR J0457-6739, MCSNR J0507-7110, MCSNR J0510-6708, MCSNR -J0512-6716, and MCSNR J0527-7134 (for more details, see Table 2 and Section 3.1).

We searched all available optical, radio, and X-ray surveys in order to secure the most complete population of LMC SNRs. Primarily, we classified the 15 LMC SNR candidates based on the well-established criteria described in Filipovic et al. (1998). We emphasize that all these sources require further study in order to secure a bona fide classification as SNRs. In Figures 1–3 we show images of the 14 LMC SNR candidates at various frequencies. An image of MCSNR J0507-6846 is shown in Chu et al. (2000). SNR extent is primarily measured using MCELS images, with some additional information obtained via *Chandra XMM-Newton* or *ROSAT* surveys when needed. Because of their very low surface brightness, we could not measure radio emission from 6 of these 15 LMC SNRs candidates.

All of the radio flux density measurements of the LMC SNRs and SNR candidates are shown here for the first time, and their associated errors are well below 10%. We determined source diameters from the highest resolution image available including optical and X-ray images. We estimated that the error in diameter is smaller than 2'' or ~ 0.5 pc. We found that our diameters estimated here are $\sim 10\%$ smaller compared to Maggi et al. (2016). The reason for this small discrepancy is because of a better resolution images that we used here compared to *XMM*. Also, we show here, for the first time, a compilation of estimated LMC SNR ages using various methods. Therefore, Table 1 is a compilation of our own measurements as well as those of other papers for this well-established sample of LMC SNRs.

3.1. Notes on the LMC SNR Candidates

MCSNR J0447-6918 (Figure 1; top left)—A large optical shell ($245'' \times 245''$) was present with an enhanced [S II]/H α ratio of >0.4 . Also, some weak 20 cm emission was detected in the NE part but no reliable flux density estimate was possible. No sensitive X-ray coverage is available in this field.

MCSNR J0449-6903 (Figure 1; top right)—Turtle & Mills (1984) originally proposed this source to be an SNR exemplifying the typical evolved shell-type SNR morphology. Although there was no obvious optical identification in MCELS, we estimated a radio spectral index of $\alpha = -0.50 \pm 0.01$ using measured flux densities of 108 mJy, 83 mJy, and 45 mJy at 36 cm (843 MHz), 20 cm (1377 MHz), and 6 cm (4800 MHz), respectively. Unfortunately, no sensitive X-ray coverage is available at this point.

MCSNR J0456-6950 (Figure 1; middle left)—This source is a potential radio SNR based on a shell-like radio structure. We have no definite optical confirmation, and X-ray surveys have not covered this region.

MCSNR J0457-6923 (Figure 1; middle right)—This source was classified as a potential optical SNR based on an [S II]/H α ratio of >0.4 as well as an evident radio emission. No sensitive X-ray coverage is available.

MCSNR J0457-6739 (Figure 1; bottom left)—This object exhibits a shell-like optical nebula with a somewhat enhanced [S II]/H α ratio of ~ 0.4 and a shell-like radio-continuum morphology. However, we were only able to measure a flux density at 20 cm of 25.9 mJy. No sensitive X-ray coverage is available.

Table 1
59 Confirmed SNRs in the LMC

Name MCSNR J	Other Name	R.A. (J2000)	Decl. (J2000)	$D_{\text{maj}} \times D_{\text{min}}$ ($''$)	PA ($^{\circ}$)	D_{av} (pc)	$\alpha \pm \Delta\alpha$	$S_{1\text{GHz}}$ (Jy)	$\Sigma_{1\text{GHz}} (\times 10^{-20})$ ($\text{W m}^{-2}\text{Hz}^{-1}\text{sr}^{-1}$)	Type	Age $\pm \Delta\text{Ages}^a$ (yr)
0448-6700	HP 460	04 ^h 48 ^m 26 ^s .3	-67°00'24"	290 × 196	135	57.9	-0.11 ± 0.05	0.0334	0.0317	X	...
0449-6920		04 ^h 49 ^m 22 ^s .3	-69°20'25"	115 × 115	0	27.9	-0.40 ± 0.08	0.0869	0.3560	X	...
0450-7050		04 ^h 50 ^m 23 ^s .5	-70°50'23"	535 × 340	30	103.4	-0.41 ± 0.03	0.6893	0.2050	CCq	70000 ± 25000 ¹
0453-6655	N4D	04 ^h 53 ^m 14 ^s .0	-66°55'10"	222 × 263	15	58.6	-0.58 ± 0.06	0.1116	0.1040	X	...
0453-6829	LHG 1	04 ^h 53 ^m 37 ^s .2	-68°29'28"	120 × 123	20	29.4	-0.34 ± 0.01	0.2100	0.7730	CCpwn	13500 ± 1500 ²
0454-6712	N9	04 ^h 54 ^m 33 ^s .0	-67°12'50"	140 × 120	0	31.4	-0.51 ± 0.03	0.0767	0.2470	TN	29500 ± 7500 ³
0454-6625	N11 L	04 ^h 54 ^m 49 ^s .9	-66°25'36"	95 × 68	45	19.4	-0.50 ± 0.03	0.1539	1.3000	CCq	11000 ± 4000 ⁴
0455-6839	N86	04 ^h 55 ^m 43 ^s .7	-68°39'02"	279 × 213	170	59.1	-0.51 ± 0.04	0.3345	0.3050	X	53000 ± 33000 ⁴
0459-7008	N186D	04 ^h 59 ^m 57 ^s .3	-70°08'07"	116 × 116	0	28.1	CCq	11000 ⁵
0505-6752	DEM L71	05 ^h 05 ^m 41 ^s .9	-67°52'39"	88 × 61	170	17.8	-0.60 ± 0.02	0.0087	0.0882	TN	4360 ± 290 ⁶
0505-6801	N23	05 ^h 05 ^m 54 ^s .1	-68°01'42"	97 × 92	20	23.0	-0.60 ± 0.04	0.3926	2.3700	CC	4600 ± 1200 ⁷
0506-6542	DEM L72	05 ^h 06 ^m 08 ^s .2	-65°42'10"	410 × 360	50	93.1	X	115000 ± 35000 ⁸
0506-7025	DEM L80	05 ^h 06 ^m 47 ^s .9	-70°25'38"	183 × 157	17	41.2	TN	19000 ± 2000 ⁹
0508-6902	HP 791	05 ^h 08 ^m 33 ^s .9	-69°02'40"	302 × 234	30	64.5	TN	22500 ± 2500 ¹⁰
0508-6830		05 ^h 08 ^m 49 ^s .5	-68°30'41"	138 × 108	45	29.8	TN	20000 ¹¹
0508-6843	N103B	05 ^h 08 ^m 59 ^s .4	-68°43'35"	27 × 29	0	6.8	-0.65 ± 0.03	0.5780	39.700	TN	860 ¹²
0509-6731	LHG 14	05 ^h 09 ^m 31 ^s .1	-67°31'17"	32 × 29	0	7.4	-0.73 ± 0.02	0.0974	5.7200	TN	310 ± 120 ¹³
0511-6759		05 ^h 11 ^m 10 ^s .7	-67°59'07"	228 × 216	0	53.8	TN	20000 ¹¹
0512-6707	HP 483	05 ^h 12 ^m 28 ^s .8	-67°07'15"	55 × 45	0	12.1	-0.49 ± 0.01	0.1046	2.2900	TN	3150 ± 1250 ¹⁴
0513-6912	N112	05 ^h 13 ^m 14 ^s .4	-69°12'15"	245 × 200	135	53.7	-0.52 ± 0.09	0.2423	0.2680	X	3500 ± 1500 ¹⁵
0514-6840	HP 700	05 ^h 14 ^m 15 ^s .5	-68°40'14"	220 × 220	0	53.2	X	...
0517-6759	HP 607	05 ^h 17 ^m 10 ^s .2	-67°59'03"	324 × 210	40	63.2	X	...
0518-6939	N120A	05 ^h 18 ^m 43 ^s .5	-69°39'11"	85 × 102	0	22.7	-0.61 ± 0.03	0.4504	2.7900	CCq	7300 ¹⁶
0519-6902	LHG 26	05 ^h 19 ^m 34 ^s .8	-69°02'06"	36 × 33	0	8.3	-0.64 ± 0.02	0.1316	6.0900	TN	600 ± 200 ¹⁷
0519-6926	LHG 27	05 ^h 19 ^m 45 ^s .3	-69°26'01"	140 × 110	30	30.1	-0.53 ± 0.03	0.1606	0.5650	X	...
0521-6542	DEM L142	05 ^h 21 ^m 38 ^s .8	-65°42'58"	135 × 141	0	33.4	X	...
0523-6753	N44I	05 ^h 23 ^m 06 ^s .5	-67°53'09"	230 × 230	0	55.8	CCq	18000 ¹⁸
0524-6623	N48E	05 ^h 24 ^m 18 ^s .9	-66°23'33"	145 × 145	0	35.1	-0.41 ± 0.02	0.0725	0.1870	CCq	...
0525-6938	N132D	05 ^h 25 ^m 02 ^s .7	-69°38'33"	114 × 90	30	24.5	-0.65 ± 0.04	5.2642	27.900	CC	3150 ± 200 ¹⁹
0525-6559	N49B	05 ^h 25 ^m 24 ^s .9	-65°59'18"	155 × 155	0	37.6	-0.56 ± 0.03	0.6344	1.4300	CC	10000 ²⁰
0526-6605	N49A	05 ^h 26 ^m 00 ^s .1	-66°05'00"	75 × 75	0	18.2	-0.59 ± 0.03	1.6618	16.000	CCq	4800 ²¹
0527-6912	LHG 40	05 ^h 27 ^m 39 ^s .3	-69°12'07"	157 × 123	80	33.8	CCq	...
0527-6549	DEM L204	05 ^h 27 ^m 54 ^s .9	-65°49'49"	335 × 275	45	73.6	-0.51 ± 0.04	0.1365	0.0803	X	...
0528-7104	HP 1234	05 ^h 28 ^m 04 ^s .3	-71°04'40"	328 × 234	155	67.1	X	25000 ²²
0528-6726	DEM L205	05 ^h 28 ^m 11 ^s .1	-67°26'49"	260 × 180	30	52.4	CCq	33500 ± 3500 ²³
0528-6713	HP 498	05 ^h 28 ^m 18 ^s .5	-67°13'49"	216 × 216	0	52.4	-0.28 ± 0.09	0.1113	0.1290	X	...
0529-6653	DEM L214	05 ^h 29 ^m 51 ^s .0	-66°53'27"	137 × 128	0	29.1	-0.68 ± 0.03	0.0863	0.2670	X	...
0530-7007	DEM L218	05 ^h 30 ^m 40 ^s .4	-70°07'27"	215 × 180	45	47.7	-0.27 ± 0.01	0.0718	0.1010	TNq	...
0531-7100	N206	05 ^h 31 ^m 57 ^s .9	-71°00'16"	190 × 170	90	43.6	-0.66 ± 0.03	0.4086	0.6850	CCpwn	25000 ± 2000 ²⁴
0532-6731	N56	05 ^h 32 ^m 19 ^s .9	-67°31'37"	180 × 180	0	43.6	-0.63 ± 0.04	0.2152	0.3600	X	...
0533-7202	RASS 236	05 ^h 33 ^m 51 ^s .0	-72°02'50"	200 × 160	45	43.5	-0.47 ± 0.06	0.1333	0.2250	TNq	23000 ± 5000 ²⁴
0534-6955	LHG 53	05 ^h 34 ^m 00 ^s .8	-69°55'08"	120 × 110	155	27.2	-0.51 ± 0.01	0.0889	0.3820	TN	10100 ²⁶
0534-7033	DEM L238	05 ^h 34 ^m 23 ^s .0	-70°33'25"	222 × 158	190	45.4	-0.44 ± 0.09	0.0796	0.1230	TN	12500 ± 2500 ²⁷
0535-6916	SNR1987A	05 ^h 35 ^m 28 ^s .0	-69°16'12"	1.8 × 1.8	0	0.4	-0.68 ± 0.03	0.8200	13700	CC	30
0535-6602	N63A	05 ^h 35 ^m 43 ^s .8	-66°02'13"	81 × 67	45	17.8	-0.74 ± 0.02	1.8641	18.700	CCq	3500 ± 1500 ²⁸
0535-6918	Honeycomb	05 ^h 35 ^m 45 ^s .5	-69°18'08"	91 × 59	160	17.7	-0.71 ± 0.05	0.1483	1.5200	X	...
0536-6735	N59B	05 ^h 36 ^m 04 ^s .2	-67°35'11"	147 × 125	35	32.9	CCpwn	60000 ± 10000 ²⁹

Table 1
(Continued)

Name MCSNR J	Other Name	R.A. (J2000)	Decl. (J2000)	$D_{\text{maj}} \times D_{\text{min}}$ ($''$)	PA ($^{\circ}$)	D_{av} (pc)	$\alpha \pm \Delta\alpha$	$S_{1\text{GHz}}$ (Jy)	$\Sigma_{1\text{GHz}} (\times 10^{-20})$ ($\text{W m}^{-2}\text{Hz}^{-1}\text{sr}^{-1}$)	Type	Age $\pm \Delta\text{Ages}^{\text{a}}$ (yr)
0536-7038	DEM L249	05 ^h 36 ^m 06 ^s .6	−70°38′38″	187 × 127	25	37.4	−0.52 ± 0.06	0.0699	0.1600	TN	12500 ± 2500 ²⁷
0536-6913		05 ^h 36 ^m 17 ^s .0	−69°13′28″	66 × 66	0	16.0	CC	3550 ± 1350 ³⁰
0537-6627	DEM L256	05 ^h 37 ^m 30 ^s .3	−66°27′45″	210 × 165	45	45.1	−0.47 ± 0.06	0.0729	0.1140	X	50000 ⁸
0537-6910	30 Dor B	05 ^h 37 ^m 45 ^s .6	−69°10′20″	136 × 116	155	30.4	−0.38 ± 0.03	2.8817	9.9000	CCpwn	5000 ³¹
0540-6944	N159	05 ^h 40 ^m 00 ^s .0	−69°44′06″	120 × 90	90	25.2	CC	18000 ³²
0540-6919	N158A	05 ^h 40 ^m 11 ^s .3	−69°19′54″	67 × 58	0	15.1	−0.63 ± 0.03	1.0272	14.300	CCpwn	1100 ± 340 ³³
0541-6659	HP 456	05 ^h 41 ^m 51 ^s .5	−66°59′03″	300 × 272	45	69.2	X	23000 ³⁴
0543-6900	DEM L299	05 ^h 43 ^m 02 ^s .2	−69°00′00″	226 × 226	0	54.9	X	10800 ± 7300 ³⁵
0547-6942	DEM L316B	05 ^h 47 ^m 00 ^s .0	−69°42′50″	200 × 160	115	43.4	−0.53 ± 0.16	0.7282	1.2300	CCq	40500 ± 1500 ³⁶
0547-6941	DEM L316A	05 ^h 47 ^m 20 ^s .9	−69°41′27″	122 × 118	140	29.1	−0.54 ± 0.16	0.5217	1.9600	TNq	33000 ± 6000 ³⁷
0547-7024	LHG 89	05 ^h 47 ^m 48 ^s .8	−70°24′52″	120 × 105	0	27.2	−0.56 ± 0.03	0.0632	0.2720	X	7100 ⁹
0550-6823	DEM L328	05 ^h 50 ^m 30 ^s .7	−68°23′37″	373 × 282	95	78.6	−0.41 ± 0.02	0.6495	0.3350	CCq	...

Note. This is a compilation of our own measurements and measurements taken from the literature. The types listed are as follows: TN—Thermonuclear (type Ia) SNR, CC—Core-Collapse SNR, CCpwn—Core-Collapse SNR with associated PWN and X—unknown type. Types listed with a “q” (e.g., CCq, TNq, etc.) are questionable and/or candidates for that type.

^a References for LMC SNRs ages: ¹Williams et al. (2004), ²Williams et al. (2004), ³Seward et al. (2006), ⁴Williams et al. (1999), ⁵Jaskot et al. (2011), ⁶Ghavamian et al. (2003), ⁷Hughes et al. (2006), ⁸Klimek et al. (2010), ⁹Maggi et al. (2016), ¹⁰Bozzetto et al. (2014b), ¹¹Maggi et al. (2014), ¹²Hughes et al. (1995), ¹³Hovey et al. (2015), ¹⁴Reid et al. (2015), ¹⁵Desai et al. (2010), ¹⁶Rosado et al. (1993), ¹⁷Borkowski et al. (2006b), ¹⁸Williams et al. (2006), ¹⁹Borkowski et al. (2007), ²⁰Park et al. (2003), ²¹Park et al. (2012), ²²Kavanagh et al. (2013), ²³Maggi et al. (2012), ²⁴Williams et al. (2005), ²⁵Kavanagh et al. (2015c), ²⁶Hendrick et al. (2003), ²⁷Borkowski et al. (2006a), ²⁸Warren et al. (2003), ²⁹Seward et al. (2012), ³⁰Kavanagh et al. (2015a), ³¹Seward et al. (2010), ³²Seward et al. (2010), ³³Crawford et al. (2014), ³⁴Grondin et al. (2012), ³⁵Warth et al. (2014), ³⁶Nishiuchi et al. (2001), ³⁷Williams & Chu (2005),

Table 2
Details of the 15 Candidate SNRs in the LMC

Name MCSNR J	R.A. (J2000)	Decl. (J2000)	$D_{\text{maj}} \times D_{\text{min}}$ (")	PA ($^{\circ}$)	D_{av} (pc)	$\alpha \pm \Delta\alpha$	$S_{1\text{GHz}}$ (Jy)	$\Sigma_{1\text{GHz}} (\times 10^{-20})$ ($\text{W m}^{-2}\text{Hz}^{-1}\text{sr}^{-1}$)	Reference & Other Names
0447-6918*	04 ^h 47 ^m 09 ^s .7	-69°18'58"	245 × 245	0	59.4	
0449-6903	04 ^h 49 ^m 34 ^s .0	-69°03'34"	135 × 135	0	32.7	-0.50 ± 0.01	0.0984	0.2926	1
0456-6950*	04 ^h 56 ^m 30 ^s .3	-69°50'47"	180 × 180	0	43.6	
0457-6923	04 ^h 57 ^m 07 ^s .8	-69°23'58"	180 × 120	90	35.6	2
0457-6739*	04 ^h 57 ^m 33 ^s .0	-67°39'05"	150 × 150	0	36.4	-0.5 [‡]	0.0304 [‡]	0.0732 [‡]	
0506-6815	05 ^h 06 ^m 05 ^s .3	-68°15'47"	255 × 210	30	56.1	0.00 ± 0.41	0.0371	0.0037	2; [HP99] 635
0507-7110*	05 ^h 07 ^m 35 ^s .3	-71°10'15"	270 × 270	0	65.4	DEM L81
0507-6847	05 ^h 07 ^m 36 ^s .0	-68°47'48"	600 × 400	80	118.8	3
0510-6708*	05 ^h 10 ^m 11 ^s .4	-67°08'04"	120 × 120	0	29.1	-0.5 [‡]	0.0029 [‡]	0.0110 [‡]	
0512-6716*	05 ^h 12 ^m 24 ^s .7	-67°16'55"	240 × 210	45	54.5	
0513-6731	05 ^h 13 ^m 29 ^s .6	-67°31'52"	150 × 105	60	30.4	-0.56 ± 0.41	0.0261	0.0897	2; [HP99] 544
0513-6724	05 ^h 13 ^m 40 ^s .0	-67°24'20"	150 × 150	0	36.4	-0.61 ± 0.41	0.0279	0.0673	2; [HP99] 530
0527-7134*	05 ^h 27 ^m 48 ^s .5	-71°34'06"	180 × 145	45	39.2	-0.52 ± 0.41	0.0284	0.0589	
0538-6921	05 ^h 38 ^m 12 ^s .9	-69°21'41"	169 × 169	0	41.0	-0.59 ± 0.04	0.5207	0.9878	1
0539-7001	05 ^h 39 ^m 36 ^s .2	-70°01'44"	210 × 120	45	38.5	-0.47 ± 0.41	0.0054	0.0115	2; [HP99] 1063

Note. New SNR candidates are marked with *. We assume $\alpha = -0.5$ for MCSNR J0457-6739 and MCSNR J0510-6708 (marked with ‡). References in Column 10 are 1—Turtle & Mills (1984), 2—HP99, and 3—Chu et al. (2000).

MCSNR J0506-6815 = [HP99] 635 (Figure 1; bottom right)—HP99 recorded an object at this position, giving it the name [HP99] 635.¹¹ They listed an extent of 31''.3 (very low likelihood), and estimated HR1 and HR2 values of 1.00 ± 0.76 and -0.05 ± 0.19 , respectively. Therefore, the X-ray source could be a point source unrelated to the SNR candidate. Although there was no optical (MCELS) signature, we detected extended radio-continuum emission and estimated flux densities of 37 mJy at both frequencies (36 cm and 20 cm), pointing to a flat spectral index, which is indicative of a PWN. This object is classified as an SNR candidate primarily based on its radio and optical morphology as the X-ray emission association is not clear at this point.

MCSNR J0507-6847—Chu et al. (2000) observed this source, consisting of a large ring of diffuse X-ray emission, and proposed it as an SNR candidate. They found an X-ray luminosity within the range expected for SNRs, and predicted an age of $\sim 5 \times 10^4$ yr based on the Sedov solution. Blair et al. (2006) did not detect this object in their far-UV survey of the MCs. We did not detect associated optical (MCELS) or radio-continuum features in this large object, and we propose that this object might represent a superbubble similar to 30 Dor C (Sano et al. 2017).

MCSNR J0507-7110=DEM L81 (Figure 2; top left)—Davies et al. (1976) listed this object as DEM L81, describing the source as a faint semicircular arc extending 4'.5. We identified a southern arc in the MCELS images ahead of the extended radio-continuum emission. As the whole source is very complex, we could not measure any flux density at our radio frequencies. However, the source appears stronger at lower frequencies and is indicative of a steep non-thermal radio-continuum spectrum. Also, there is no sensitive X-ray coverage in this field.

MCSNR J0510-6708 (Figure 2; top right)—We determined an enhanced [S II]/H α ratio of >0.5 in the shell. The radio-continuum emission is centrally located and very weak ($S_{20\text{cm}} = 2.5$ mJy). At present, there is no sensitive X-ray coverage in the direction of this object.

MCSNR J0512-6716 (Figure 2; middle left)—A prominent X-ray ring from *XMM-Newton* images can be seen with some very weak radio emission overlapping. We could not confirm optical identification of this object.

MCSNR J0513-6731 = [HP99] 544 (Figure 2; middle right)—HP99 named this object [HP99] 544, recording an extent of 27''.4, in addition to an HR1 measurement of 1.00 ± 0.29 . A low likelihood for the extent leaves the possibility of an X-ray point source unrelated to the SNR candidate. We detected a weak but distinctive [O III] emission surrounding a distinct radio source. The spectral index was determined to be $\alpha = -0.56$, based on measured flux densities of 28.7 mJy at 36 cm and 21.5 mJy at 20 cm.

MCSNR J0513-6724 = [HP99] 530 (Figure 2; bottom left)—HP99 gave this object the name [HP99] 530, recording an extent of 17''.5, in addition to HR1 and HR2 ratios of 1.00 ± 0.21 and 0.15 ± 0.17 , respectively. Because these hardness ratios suggest a “hard” source and also given the low source extent likelihood, HP99 suggest the source could be unrelated to the SNR candidate. We found a strong radio point source with flux densities of 31 mJy (at 36 cm) and 23 mJy (at 20 cm), implying a non-thermal spectral index of $\alpha = -0.61$. There is also a weak [S II] ring, although somewhat smaller than the X-ray extent.

MCSNR J0527-7134 (Figure 2; bottom right)—We classified this object as an SNR candidate based on an enhanced [S II]/H α ratio of >0.4 as well as a shell-like radio-continuum morphology. We estimated flux densities of 31 mJy (at 36 cm) and 24 mJy (at 20 cm), implying a non-thermal spectral index of $\alpha = -0.52$. This candidate was observed very recently with *XMM-Newton* (2016 October, PI: P. Kavanagh). The detection of soft X-ray emission, correlated with the optical and radio shells, suggests that this source is a bona fide SNR. A detailed study of MCSNR J0527-7134 will be presented elsewhere.

MCSNR J0538-6921 (Figure 3; left)—Turtle & Mills (1984) originally proposed this source to be an SNR. This is the only strong LMC SNR candidate to date that has been detected in radio frequencies alone. The estimated spectral index is $\alpha = -0.59 \pm 0.04$, based on measured flux densities at various frequencies.

¹¹ [HP99] xxx is SIMBAD nomenclature with source number xxx from HP99.

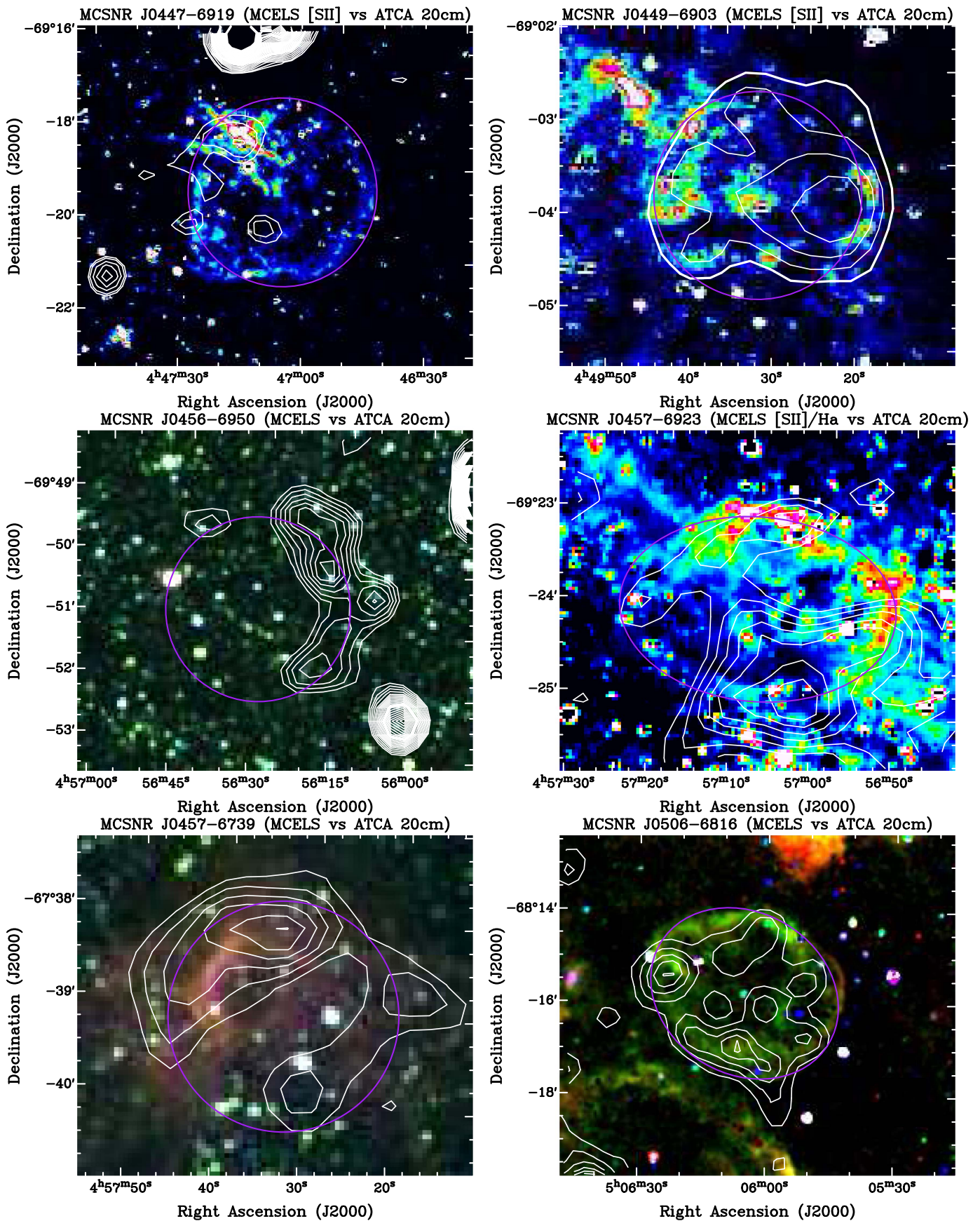


Figure 1. LMC SNR candidates 1. Color images are MCELS, where RGB corresponds to $H\alpha$, [S II], and [O III]. The color image of MCSNR J0457-6923 is the ratio map between [S II] and $H\alpha$. Contours are from the ATCA 20 cm mosaic survey and start at the 3σ local noise level with a spacing of 1σ . The circles/ellipses (purple) represent the approximate extent of the SNR candidates.

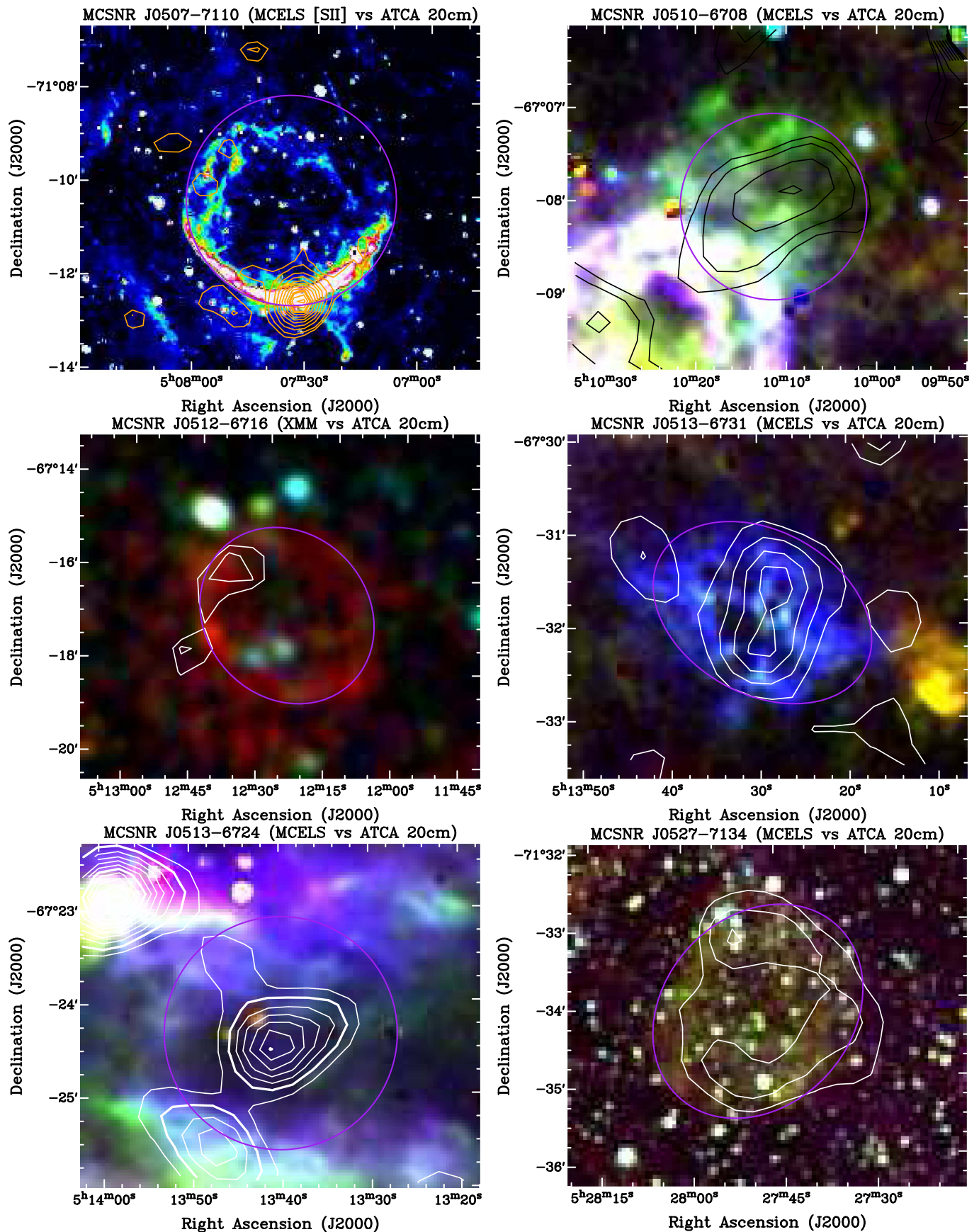


Figure 2. LMC SNR candidates 2. Color images are MCELS, where RGB corresponds to $H\alpha$, [S II], and [O III]. The MCSNR J0512-6716 color image is from the *XMM-Newton* X-ray survey of LMC SNRs (Kavanagh et al. 2015b). Contours are from the ATCA 20 cm mosaic survey and start at the 3σ local noise level with a spacing of 1σ . The circles/ellipses (purple) represent the approximate extent of the SNR candidates.

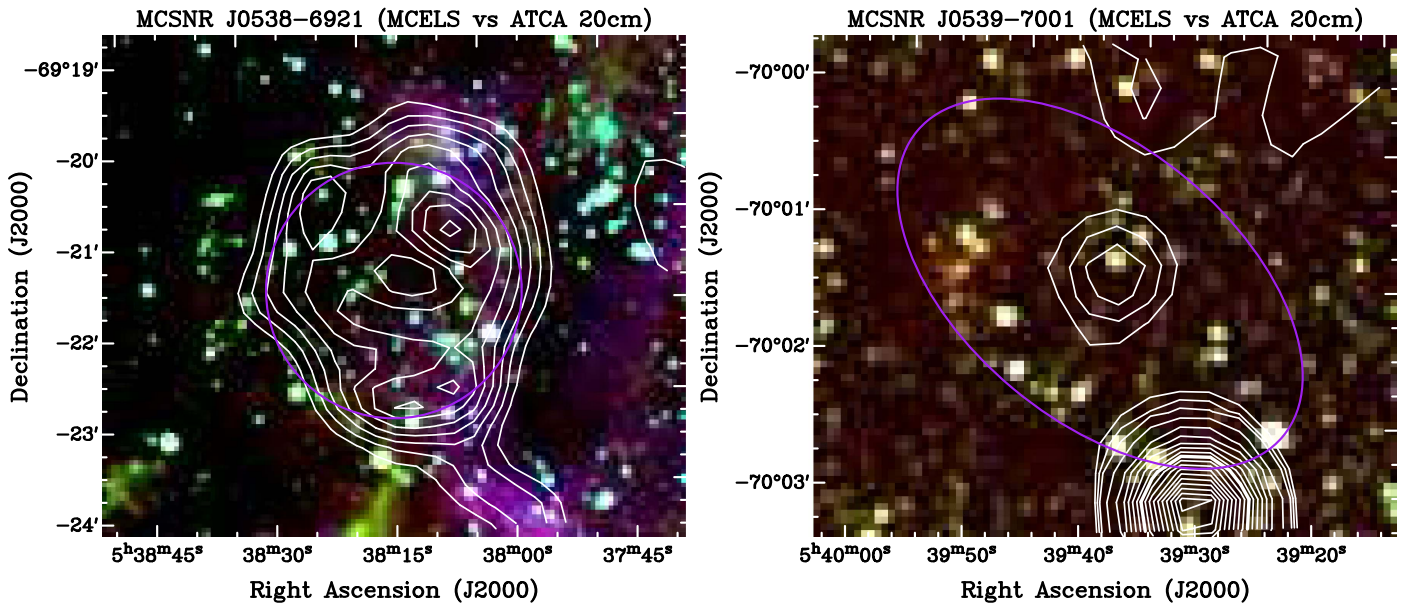


Figure 3. LMC SNR candidates. Color images are MCELS where RGB corresponds to H α , [S II], and [O III]. Contours are from the ATCA 20 cm mosaic survey and start at the 3σ local noise level with a spacing of 1σ . The ellipses (purple) represent the approximate extent of the SNR candidates.

MCSNR J0539-7001 = [HP99] 1063 (Figure 3; right)—HP99 assigned this source the name [HP99] 1063, recording an extent of $18''.2$, in addition to listing HR1 and HR2 values of 1.00 ± 0.17 and -0.17 ± 0.10 , respectively. They classified the X-ray source, which was constant in flux during the *ROSAT* observations, as an SNR candidate. We found a weak radio point source in the center of this remnant with measured flux densities at 36 cm of 5.8 mJy and at 20 cm of 4.6 mJy, giving a spectral index of $\alpha = -0.47$.

4. Physical Properties from Kernel Density Estimates

This most complete sample of LMC SNRs allows us to better study their morphology, evolution, and physical processes that are responsible for their observed emission. To get better statistical insight into the physical properties of the LMC SNRs, we reconstructed the probability density functions (PDF) for the diameter, flux density, spectral index, and ovality. We note that the errors associated with the diameter ($<2''$) and flux density ($<10\%$) are small and thus not displayed in this analysis. For n independent and identically distributed (iid) measurements of a variable $X(x_1, x_2, x_3, \dots, x_n)$, the PDF ($f(x)$) is reconstructed using the Gaussian kernel smoothing (Sheather 2004; Wasserman 2010; Feigelson & Babu 2012), with the kernel function

$$K\left(\frac{x - x_i}{h}\right) = \frac{1}{\sqrt{2\pi}} \exp\left(-\frac{(x - x_i)^2}{2h^2}\right). \quad (1)$$

The common way to select the kernel bandwidth h and obtain the $f(x)$ estimate $f_h(x)$,

$$f_h(x) = \frac{1}{nh} \sum_{i=1}^n K\left(\frac{x - x_i}{h}\right), \quad (2)$$

is to minimize the mean integrated square error (MISE):

$$\text{MISE}(h) = \int_{-\infty}^{\infty} (f_h(x) - f(x))^2 dx. \quad (3)$$

For a Gaussian kernel, under asymptotic conditions, $n \rightarrow \infty$ and $h \rightarrow 0$, such that $nh \rightarrow \infty$, MISE(h) translates to the asymptotic MISE (AMISE):

$$\text{AMISE}(h) = \frac{1}{4} h^4 R(f) + \frac{h}{2\sqrt{\pi}n}, \quad (4)$$

where $R(f)$ is the roughness of f calculated as

$$R(f) = \int_{-\infty}^{\infty} f''(x)^2 dx. \quad (5)$$

It can be shown that AMISE(h) has the minimum at

$$h = (2\sqrt{\pi}nR(f))^{-0.2}. \quad (6)$$

To estimate $f''(x) = d^2f(x)/dx^2$, a “plug-in” bandwidth value h_0 is required so that $f_{h_0}''(x)$ can be calculated. Usually, a rule-of-thumb value can be used (Silverman 1986). If σ is the standard deviation of the sample of n data points, the rule-of-thumb bandwidth is calculated as $h_0 = \sigma n^{-0.2}$. This value is obtained by minimizing MISE as described above under the additional assumption that the data are normally distributed.

However, the h_0 optimal for calculating $f(x)$ need not be the optimal choice for estimating $f''(x)$. In addition, the asymptotic nature of Equation (6) may give incorrect results when there is a lot of fine structure in the data. We illustrate this in Figure 4. The AMISE data do not appear to have a noticeable minimum value.

As a more robust way of estimating h , we used a procedure similar to that described in Faraway & Jhun (1990). Instead of minimizing AMISE(h), they minimized the bootstrap MISE:

$$\text{BIMSE}(h) = B^{-1} \sum_{i=1}^B \int_{-\infty}^{\infty} (f_h^*(x) - f(x))^2 dx. \quad (7)$$

where B is the number of smooth bootstrap resamplings from the original data sample. At a given h , each resample gives $f_h^*(x)$. Unlike the common bootstrap (Efron & Tibshirani 1993), the smooth bootstrap also requires a “plug-in” bandwidth h_0 for resampling and estimating $f(x)$. To each

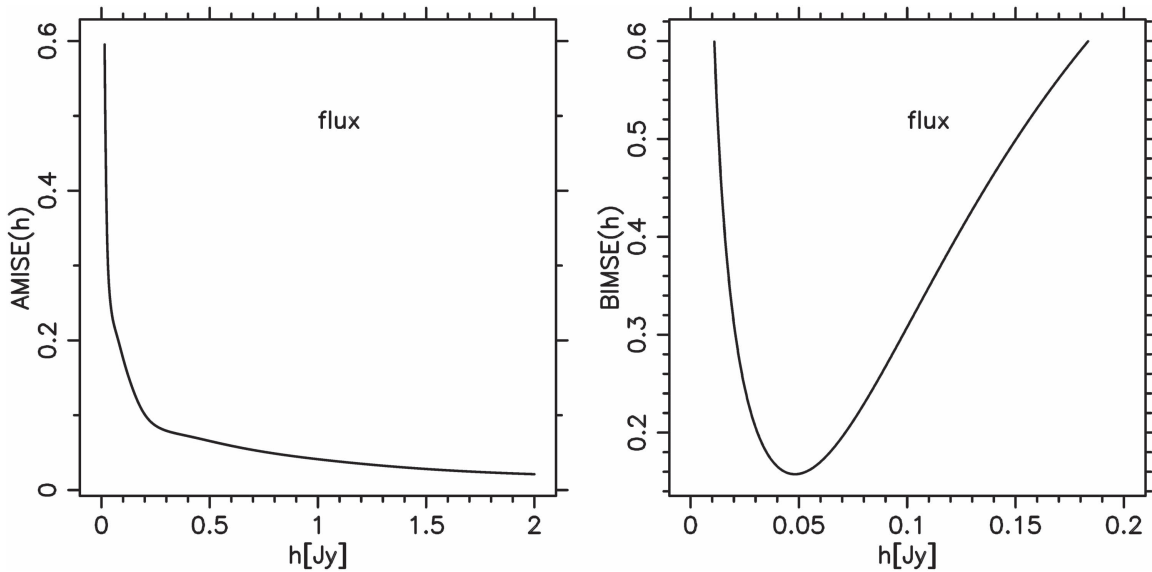


Figure 4. Asymptotic mean integrated squared error (AMISE) and bootstrap integrated mean squared error (BIMSE) for the LMC flux density data at 1 GHz, shown in Figure 17. Unlike AMISE, the BIMSE merit estimator shows a clear minimum at the h value, which is considered the optimal smoothing bandwidth.

resampled data point x_i^* , an offset is added as $x_{sb\ i}^* = x_i^* + \theta(h_0, x_i^*)$, where θ is normally distributed with standard deviation h_0 around a mean x_i^* . The $x_{sb\ i}^*$ values obtained in this manner are then used to calculate $f_h^*(x)$. The BIMSE(h) in Figure 4 is calculated with the optimal bandwidth resulting from the procedure described below, the results of which are presented in Section 6.3. Unlike AMISE, it shows a very distinctive, unambiguous, minimum value of global character. Although the BIMSE calculation is much more intensive than the calculation of AMISE, we find it significantly more robust and reliable for estimating optimal smoothing bandwidths. Since AMISE data do not appear to have a strong minimum value in many of the cases examined in this work, we adopted the BIMSE procedure, which (as evident from Figure 4) shows a distinctive BIMSE(h) minimum value even on an order of magnitude smaller scale than AMISE(h), for estimating optimal smoothing bandwidths.

4.1. Procedure Description

Using the rule-of-thumb bandwidth, we performed smooth bootstrap resamplings and estimated $f(x)$ from the original data points. To minimize BIMSE(h), we used a golden section search algorithm (Kiefer 1953), which narrows down the interval that contains the minimum value by comparing the BIMSE(h) values at four points. To reduce the influence of the Monte Carlo error on the minimizing procedure, we allowed the h values within the algorithm to change only in increments of $h_s = 10^{\mu(h_0)-2}$, where μ presents the order of magnitude of its argument. The search was stopped when the size of the h interval containing the minimum fell below h_s . At each given h value, the $f_h^*(x)$ was calculated for all resamplings and the $(f_h^*(x) - f(x))^2$ term was averaged to obtain BIMSE(h).

In the work of Faraway & Jhun (1990), the authors stated that their procedure can be used in an iterative manner and hence improve the values obtained for an optimal smoothing bandwidth. We iterated the above procedure until the difference between the input and output h values fell below h_s or until this

difference h_{dif} changes sign, in which case we took the input value h_{in} of the final iteration as the outcome of the procedure. Even in such a case, h is calculated with a $\approx \mu(h_{in}) - 1$ order of magnitude accuracy. The change of sign in h_{dif} can be avoided and the accuracy improved simply by applying a larger number of bootstrap resamplings. However, Faraway & Jhun (1990) noted that, at the time, their procedure was very computationally intensive and that they obtained satisfactory results using only 100 resamplings. The calculations described in this work took up to ≈ 1 day of computing per examined data sample on a standard desktop PC using 500 bootstrap resamplings. However, this computing time was dominated by repeating the procedure for computing confidence bands (described below), which required a much greater computation intensity. To increase the speed of the computations, we calculated the Gaussian distribution values only within the five standard deviations from the mean, considering the values outside this interval to be zero.

4.2. Confidence Bands and Parameters

Faraway & Jhun (1990) noted that a by-product of their procedure is the estimation of confidence intervals as desired quantiles of the $f_h^*(x)$ distributions, where \hat{h} is the output optimal bandwidth of their smoothed bootstrap procedure. However, the confidence band derived in this manner depends on \hat{h} , which depends on h_0 . To avoid this we applied a common bootstrap resampling (without the addition of a smoothing term θ) to the original data sample. For each of the resamples obtained in this way, we applied the described smoothed bootstrap procedure to obtain $f_{h_i}^*(x)$, where the bullet sign designates that an optimal smoothing bandwidth was obtained for the common bootstrap resample of the original data sample. At each selected point x_j along the x -axis, we then calculated the desired confidence fraction f_{ci} of the $f_{h_i}^*(x_j)$ values. First, we calculated the median of the given $f_{h_i}^*(x_j)$ array of values and then the upper and lower limits of confidence bands as the $f_{ci}/2$ fraction of the total number of array elements from the

median value. The median value was also used as the value of the smoothed density distribution $\hat{f}(x_j)$ at a point x_j .

If the testing x_{\min} and x_{\max} are the lowest and highest values of the data sample, respectively, the density distributions were calculated in the $[x_{\min} - 5 * h_0, x_{\max} + 5 * h_0]$ interval at the centers of 10^3 bins of equal width. The confidence bands are calculated as an $f_{ci} = 0.75$ fraction of the total number of 500 common bootstrap resamplings (\bullet) of the original data sample. We also used 500 smooth bootstrap resamplings ($*$) for each (\bullet) resampling. For each (\bullet) distribution, we calculated the mean, mode, and median. The uncertainties of the mean, mode, and median were calculated similarly to the confidence bands for the smooth density distribution, and we give the confidence band with the higher discrepancy from the median as the uncertainty. Confidence bands were also obtained at $f_{ci} = 0.75$, similar to $\hat{f}(x_j)$. The smooth density functions, with their parameters obtained as described above, for diameter, radio flux, spectral index, and ovality, are presented in Section 5.

4.3. Kernel Density Smoothing in 2D

A similar procedure to that described in this section can be generalized to a 2D case. We applied the procedure in 2D to the LMC and SMC radio surface brightness and diameter data to check if there were any significant emergent data features (Figure 20). The generalization of the procedure can be done in two ways, either by using a 2D Gaussian kernel (where a kernel is a function of two variables and two smoothing bandwidths), or as a product kernel of separate Gaussian kernels in each dimension. We adopted the latter. As described in Feigelson & Babu (2012), for a 2D case, the density estimate in (x, y) space is calculated as

$$f_{h^x h^y}(x, y) = \frac{1}{nh^x h^y} \sum_{i=1}^n K\left(\frac{x - x_i}{h^x}\right) K\left(\frac{y - y_i}{h^y}\right), \quad (8)$$

where h^x and h^y are the bandwidths for the kernel components in x and y , respectively. For the 2D density estimate procedure, only the smoothed bootstrap was used to minimize over BIMSE. Due to higher computation requirements, we did not use common bootstrap resamplings to estimate confidence intervals. For the input values to the procedure h_0^x and h_0^y (similar to the 1D case), we used rule-of-thumb bandwidths calculated separately in each dimension. For the range of h^x and h^y we calculated and minimized BIMSE. The values of h^x and h^y where BIMSE reached a minimum were used as the next iteration input values. The procedure was repeated until the output values for h^x and h^y equal the input values at the given level of accuracy.

5. Results

Here we present a statistical analysis and discussion of the 59 confirmed (Table 1) and 15 candidate SNRs (Table 2) in the LMC (Figure 5). This includes 16 known SNRs resulting from a thermonuclear SN (type Ia) explosion and 23 confirmed to arise from a core-collapse (CC) SN event (Maggi et al. 2016, and reference therein).

5.1. Spatial Distribution

To investigate the spatial distribution of SNRs in the LMC, annotations containing the size and position angle of the 59 confirmed and 15 candidate remnants were superimposed on the HI peak temperature map from Kim et al. (1998). There is an indication of a connection between the higher HI density (also including H α and radio continuum) and the location of SNRs, which seems to follow a spiral structure (Filipovic et al. 1998). The mean foreground HI column density in the direction to the 59 confirmed and 15 candidate remnants was estimated to be $\sim 2 \times 10^{21}$ atoms cm^{-2} (with a Standard Deviation $\text{SD} = 1 \times 10^{21}$ atoms cm^{-2}), while the ‘‘empty’’ LMC 4 supershell (Bozzetto et al. 2012b) exhibits a mean HI density of 5×10^{20} atoms cm^{-2} ($\text{SD} = 1 \times 10^{20}$ atoms cm^{-2}). Curiously, we found only one SNR (MCSNR J0529-6653 inside the LMC4 supershell) to be located outside the apparent spiral structure of the HI distribution. Also, MCSNR J0527-6549 expands in a very rarified environment with a mean HI column density of 6×10^{20} atoms cm^{-2} . We note that our 16 type Ia SNR sample might be expanding in a somewhat lower density environment (mean = 1.9×10^{21} atoms cm^{-2}), while the CC sample of 23 LMC SNRs exhibits a mean HI column density of 2.4×10^{21} atoms cm^{-2} . However, SDs of both samples are quite large ($\text{SD} = 1.1 \times 10^{21}$ atoms cm^{-2}). Therefore, this is indicative of a different molecular environment in which type Ia and CC LMC SNRs are expanding, although it should be taken with caution.

5.2. Multifrequency Emission Comparison

To compare the multifrequency emission from the 59 known SNRs in the LMC, we plotted a Venn diagram (Figure 6) that summarizes the number of SNRs exhibiting emission in the different EM domains. It is important to note that the lack of detected emission does not mean that the remnant does not emit such a radiation. However, it may indicate that the emission is under the sensitivity level of current surveys. As for the candidate remnants, many of them were entangled in unrelated emission or not part of current surveys, making it difficult to construct a worthwhile Venn diagram for these sources. We also note that there are examples of SNRs such as the SMC SNR HFPK 334 (Crawford et al. 2014) or the Galactic Vela Jr SNR (Filipović et al. 2001; Stupar et al. 2005) that could not be identified in optical frequencies despite extensive searches.

For comparison to our LMC results, Venn diagrams were constructed for various other nearby galaxies, shown in Figure 7. We note that some of these galaxies do not have deep X-ray and/or radio coverage. Still, our results are closely comparable to those found for the SMC (Filipović et al. 2005), which is to be expected as it is the most similar to the LMC. The obvious common trait between the LMC and SMC SNR populations is that they are ubiquitous in X-rays because of low foreground absorption toward the MCs. We concluded from Figure 6 that this sample is not under severe influence from observational biases. Although the LMC and SMC *XMM-Newton* surveys reach similar depth, the LMC X-ray field coverage is somewhat incomplete and therefore our present LMC X-ray SNR sample is likely incomplete as well.

Comparing Figures 6 and 7, we note that all other galaxies have high numbers of detected SNRs only in optical frequencies, with small numbers of SNRs in cross-sections of the Venn diagrams. This is expected, as Pannuti et al. (2000)

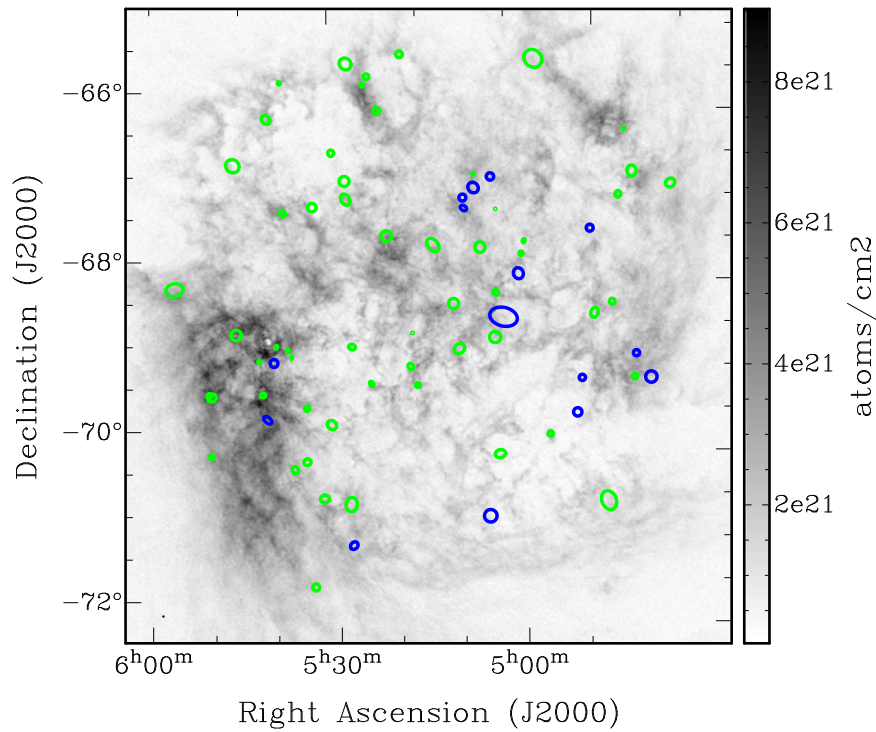


Figure 5. Spatial distribution of the 59 confirmed and 15 candidate SNRs in the LMC. There appears to be a connection between the location of the remnants and the spiral pattern of the emission from the H I peak temperature map (Kim et al. 1998, gray scale). Green symbols represent confirmed remnants, while blue symbols show the position of candidate remnants.

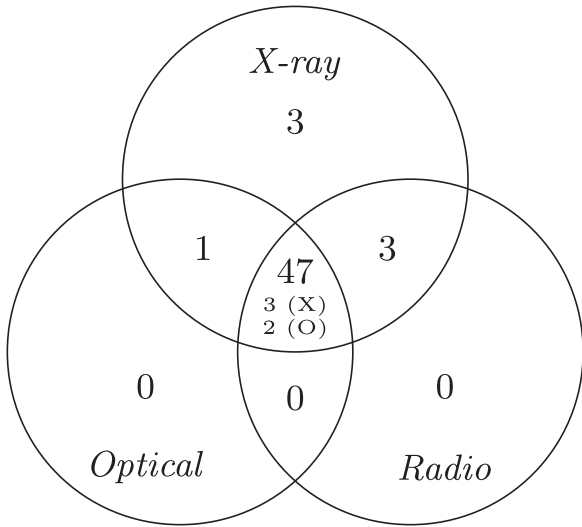


Figure 6. Venn diagram showing the 59 confirmed LMC SNRs in different electromagnetic domains. In the center pane, the 3 (X) and 2 (O), where X = X-ray and O = optical, show those remnants which either lack observations or are entangled in unassociated emission, although if present, would reside in this group.

argued that X-ray and radio SNRs are mixed/embedded and therefore confused with H II regions in distant galaxies. Also, we argue that the detection of optical SNRs in distant galaxies is biased toward lower densities. Therefore, we detect only smaller numbers of X-ray/radio SNRs in the more distant samples—ones that are brighter and in denser, star-forming regions.

Interestingly, in a revised catalog of 294 Galactic SNRs by Green (2014), 93% were detected in radio, ~40% in X-ray, and

only ~30% at optical wavelengths. This points to a clear selection bias, which limits the optical and X-ray detection. This is most likely due to obscuration from dust and clouds, as well as the lack of deeper observations at various frequencies. Also, we note that NGC 55 is an edge-on spiral galaxy and therefore, only a small number of SNRs can be detected due to obscuration.

5.3. Differential Size Distribution

To measure the extent of the SNRs in the LMC, an ellipse was fitted to delineate the bounds of emission for all confirmed and candidate SNRs in this study (Bozzetto et al. 2014b; see Figure 7). A multiwavelength approach was used and the given size takes into account the optical, radio, and X-ray emission. Such an approach was taken as some shells may appear incomplete at optical wavelengths, although complete at radio or X-ray wavelengths, and vice versa. A somewhat typical example of this is where emission in one band (e.g., X-rays) is located in the center and encased by an optical/radio shell, e.g., MCSNR J0508–6902 presented in Bozzetto et al. (2014b, Figure 2), where the radio (5500 MHz) and optical (H α) emission form the “ring” of emission, inside which the X-ray (0.7–1.1 keV) emission resides. The major and minor axes, in addition to the position angle of these measurements, are listed in Tables 1 and 2. The resulting PDF showcasing the distribution of these data is displayed in Figure 8, where the diameter was taken as the geometric average of the major and minor axes (Tables 1 and 2).

The mean value of the reconstructed distribution for the 59 confirmed and 15 candidate remnants was found to be 39 ± 4 pc for confirmed SNRs, and 41 ± 3 pc for the entire sample (Figure 8). This increased mean value for the entire sample is most likely due to many of the candidate remnants

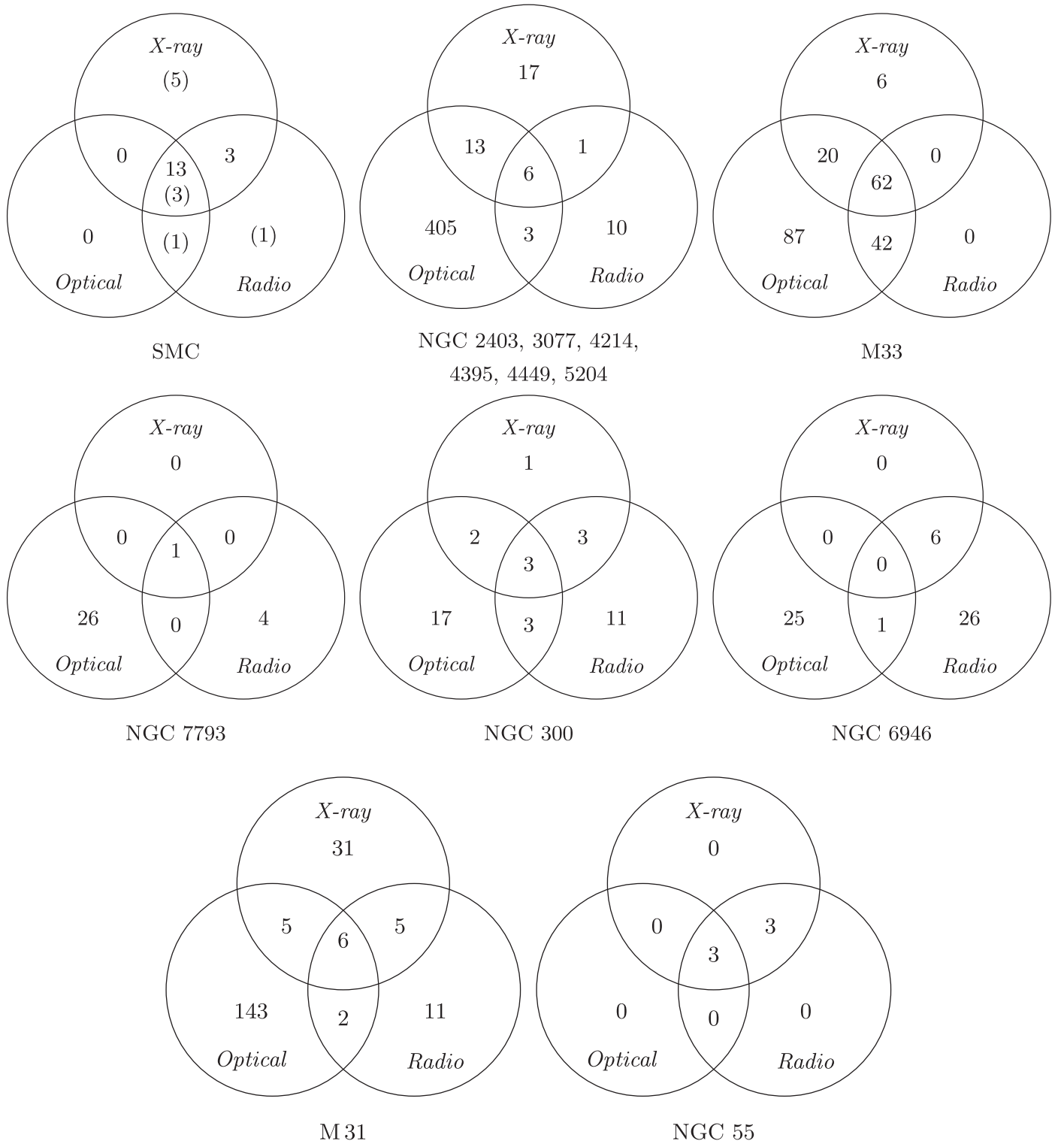


Figure 7. Series of Venn diagrams showing the detection of extragalactic SNRs in their host galaxies. The numbers in brackets denote candidate SNRs. Top row, left: data from the SMC (Filipović et al. 2005; Haberl et al. 2012). Middle: data from six galaxies (NGC 2403, 3077, 4214, 4395, 4449, and 5204 as described in Leonidaki et al. 2013). Right: data from M33 (K. Long et al. 2016, private communication). Middle row, left: data from NGC 7793 (Pannuti et al. 2011; Galvin et al. 2014). Middle: data from NGC 300 (Millar et al. 2011; Galvin et al. 2012). Right: data from NGC 6946 (Pannuti et al. 2007). Bottom row: data from M31 (Galvin & Filipovic 2014) and data from NGC 55 (O’Brien et al. 2013). We note that NGC 55 is an edge-on spiral galaxy that shows only a fraction of its SNRs due to obscuration.

being larger and weaker, only being recently detected by newer and more sensitive instruments. The majority (36 out of 59 or 61%) of the remnants were found to exhibit diameters in a range of 15–50 pc. These values are moderately larger than the

value found in the study of M83 SNRs by Dopita et al. (2010), where a mean diameter of 22.7 pc (with standard deviation of $SD = 10.3$ pc) was found for a sample of 47 remnants. Also, in a study of the SMC, Filipović et al. (2005) found a mean

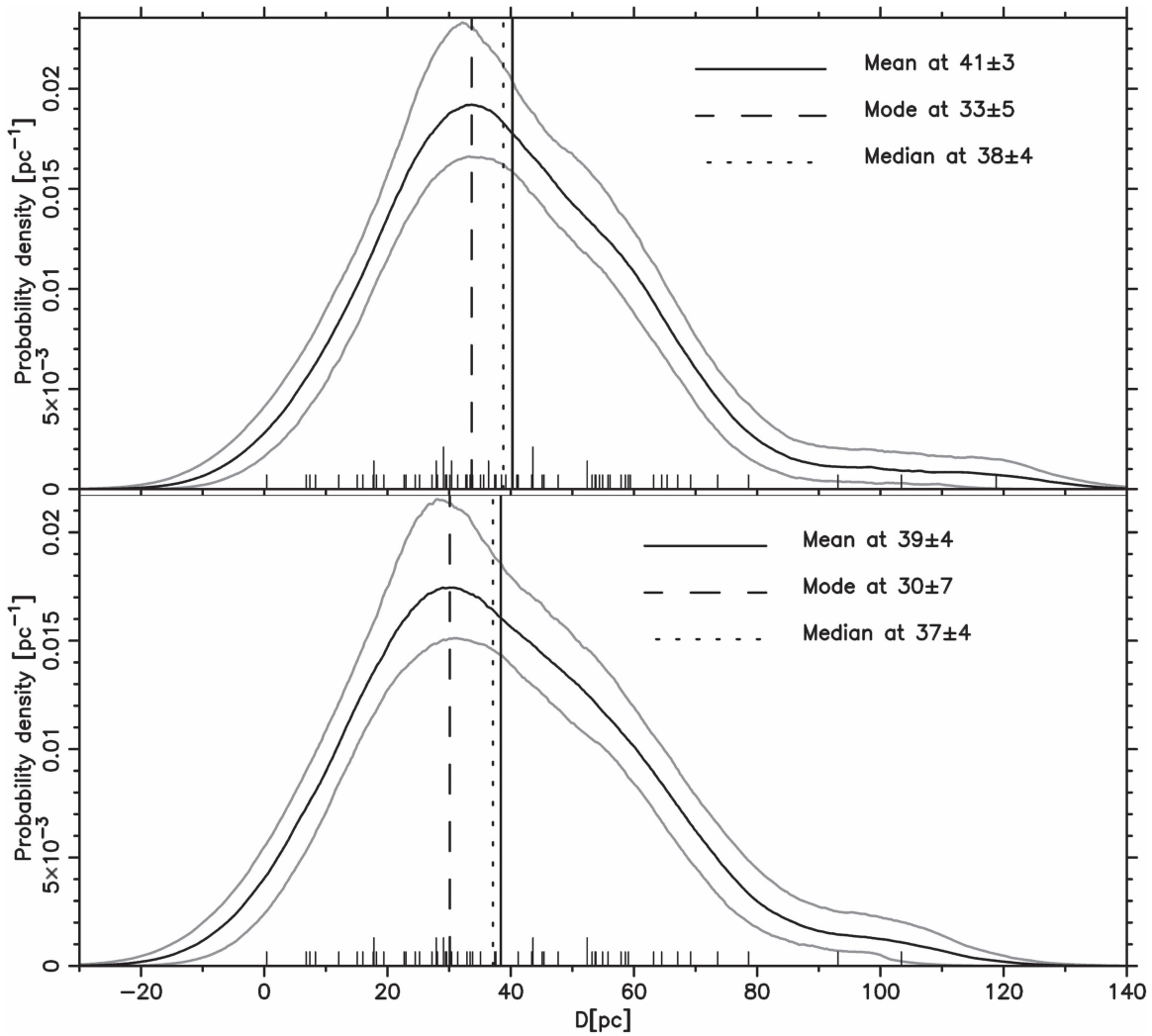


Figure 8. SNR diameter smoothed density distributions, obtained as described in Section 4, with round-up values for mean, mode, and median. The data points are marked with vertical dashes on the horizontal axis, with dash length proportional to the number of SNRs in the sample with the corresponding diameter. Distribution parts with $D < 0$ have no physical meaning and are plotted for the sake of completeness. The gray lines represent estimated uncertainties at the 75% level (as explained in Section 4.2). Top: sample of 74 confirmed and candidate LMC SNRs. Bottom: sample of 59 confirmed LMC SNRs. The optimal smoothing bandwidths for the examined data samples were found to be 11.4 pc for confirmed remnants and 9.89 pc for the bulk sample of confirmed and candidate remnants.

diameter of 30 pc, and argued that such a value indicates that most of the remnants are in the adiabatic (Sedov) evolutionary stage. The results of this study are more in line with those found by Long et al. (2010) in their study of M33, finding a median of 44 pc, and by Lee & Lee (2014) of M31, which showed a strong peak at $D = 48$ pc.

5.4. Spherical Symmetry

The spherical symmetry of the LMC SNR population was measured to investigate whether or not a trend exists between the type of SNR and how circular their morphology appeared. Lopez et al. (2011) suggested a link between the spherical thermal X-ray morphology and the remnant type, where those SNRs resulting from a type Ia SN explosion were more spherical than those from an CC SN. In this study, we define SNR spherical symmetry via

$$\text{Ovality (\%)} = \frac{2(D_{\text{maj}} - D_{\text{min}})}{D_{\text{maj}} + D_{\text{min}}}, \quad (9)$$

where D_{maj} and D_{min} are the major and minor axes, respectively. This was done for all 59 confirmed remnants using the diameter measurements shown in Table 1 (Col. 5).

We plot the smoothed density distribution for the ovality data (as explained in Section 4) in Figure 9. The large uncertainty for the mode parameter and shape of the confidence bands strongly suggest the existence of statistically significant bi-modality. To test whether this bi-modality is related to progenitor type, we plotted the smoothed density distributions for the subsamples selected by progenitor type: type Ia, CC, and unknown (with progenitor type being undetermined).

In Figure 10 the mode values for all examined subsamples overlap within the estimated uncertainties at the 75% confidence level, so it is unlikely that the examined subsamples are actually coming from statistically distinct populations of SNRs. Also, from the shapes and parameters of the distributions for type Ia and CC progenitor types, it appears that no distinction based on the progenitor type can be made and that the expected ovality of ~ 0.16 should be even smaller since the progenitors from the unknown group are more spherical in

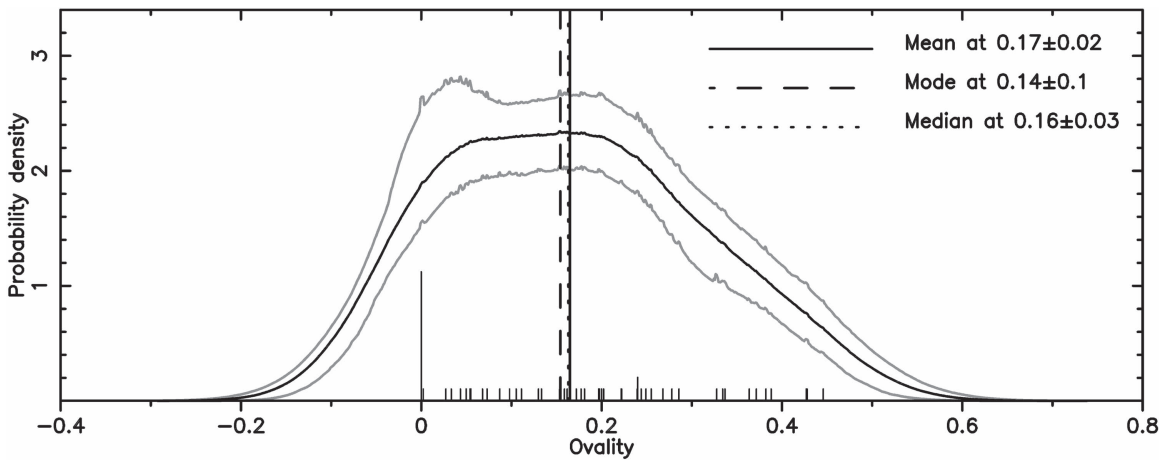


Figure 9. Smoothed density distribution for ovality, obtained as described in Section 4, with round-up values for the mean, mode, and median. The data points are marked with vertical dashes on the horizontal axis, with dash length proportional to the number of SNRs in the sample with the corresponding ovality. Distribution parts with ovality smaller than 0 have no meaning by definition and are plotted for completeness. The gray lines represent estimated uncertainties at the 75% level (as explained in Section 4.2). The optimal smoothing bandwidth for the analyzed data sample was calculated to be 0.079.

shape. In total, $\sim 27\%$ (16 out of 59) of the LMC SNRs exhibit ovality up to 5% (0–0.05) and only 2 out of 16 ($\sim 13\%$) type Ia SNRs’ ovality are within this range, which does not support the hypothesis that type Ia SNRs are more spherical in shape.

To further test if there is a statistically significant independence for ovality subsamples based on SNR progenitor type, we conducted an Anderson–Darling test (Anderson & Darling 1954), studied in more detail for a two-sample case by Pettitt (1976). The test calculates the parameter

$$A_{nm}^2 = \frac{nm}{N} \int_{-\infty}^{\infty} \frac{(F_n(x) - G_m(x))^2}{H_N(x)(1.0 - H_N(x))} dH_N(x), \quad (10)$$

where $F_n(x)$ and $G_m(x)$ are the empirical cumulative distribution functions (ECDF) for sample 1 with n points and sample 2 with m points, while $H_N(x)$ is the ECDF of a joint sample with $N = m + n$ points. The integral of the squared deviations weighted with the joint ECDF factor gives a robust measure of the difference, even at the tails of the distribution where, by definition, all ECDFs converge toward 0 and 1. The resulting value of A_{nm}^2 is then compared against the critical value of A_{nm}^2 at a specific level of confidence (α) to test the null hypothesis that the two samples represented by $F_n(x)$ and $G_m(x)$ are sampled from the same underlying distribution. The results of the test are shown in Table 3. It is apparent that even for the selected confidence limit of 0.1, $A_{nm}^2 < A_{nm}^2$, meaning that the calculated A_{nm}^2 is within the 90% confidence interval from the expected value for A_{nm}^2 . This indicates that the null hypothesis cannot be rejected at the $\alpha = 0.1$ level and that the tested subsamples could plausibly be sampled from the same distribution. This argues against the earlier stated existence of a correlation between the type of SNR and their spherical symmetry.

In addition, we make a scatter plot in Figure 11 of the geometric mean diameter versus ovality, color-coded by the ages of the remnants. For this population, there does not appear to be any conclusive evidence that the type of SN explosion (Table 1; Col. 11) correlates with the ovality (as defined here)

of the resulting SNR or its known age, estimated from the various multifrequency measurements (Table 1; Col. 12).

For the 28 LMC SNRs older than 10,000 yr (Figure 11), we found a suggestive progenitor type. This is somewhat surprising, as for older remnants, signatures of progenitor type are likely to be faint and hence harder to determine. Also, in Figure 10, the distribution of objects with undetermined progenitor type appears to be skewed toward smaller ovality values. This implies that older remnants might be more spherical in shape.

We expect that future surveys with high accuracy ovality measurements, better age determinations, and more complete samples are of crucial importance for a better assessment of this subject.

5.5. Cumulative Number–Diameter Relation

The cumulative number–diameter relation, also known as $N(<D) - D$, shows the number of SNRs smaller than a given diameter. Assuming a rough uniformity in SN explosion and environment, it is possible to estimate the evolution of SNRs and the rate of SN occurrence via

$$N(<D) = \frac{t(D)}{\tau}, \quad (11)$$

where $t(D)$ is the age of the remnant and τ is the average time between the SN events, i.e., τ^{-1} is the average supernova rate. As a remnant evolves, it is expected to pass through different phases of hydrodynamical evolution. The turnover from the free-expansion phase to the Sedov phase, i.e., when the mass of the swept-up material is higher than the ejecta, was approximated using the equation from Spitzer (1978):

$$R_{pc} \approx 2.13 \left(\frac{M_E}{n_o} \right)^{1/3}, \quad (12)$$

where R_{pc} is the transition radius in parsecs, n_o is the number density of the ISM per cubic centimeters, and M_E is the ejecta mass in solar units. If we assume progenitor masses between the Chandrasekhar limit ($1.4 M_{\odot}$) and that of a large star ($40 M_{\odot}$) expanding in ambient densities between 0.1 and

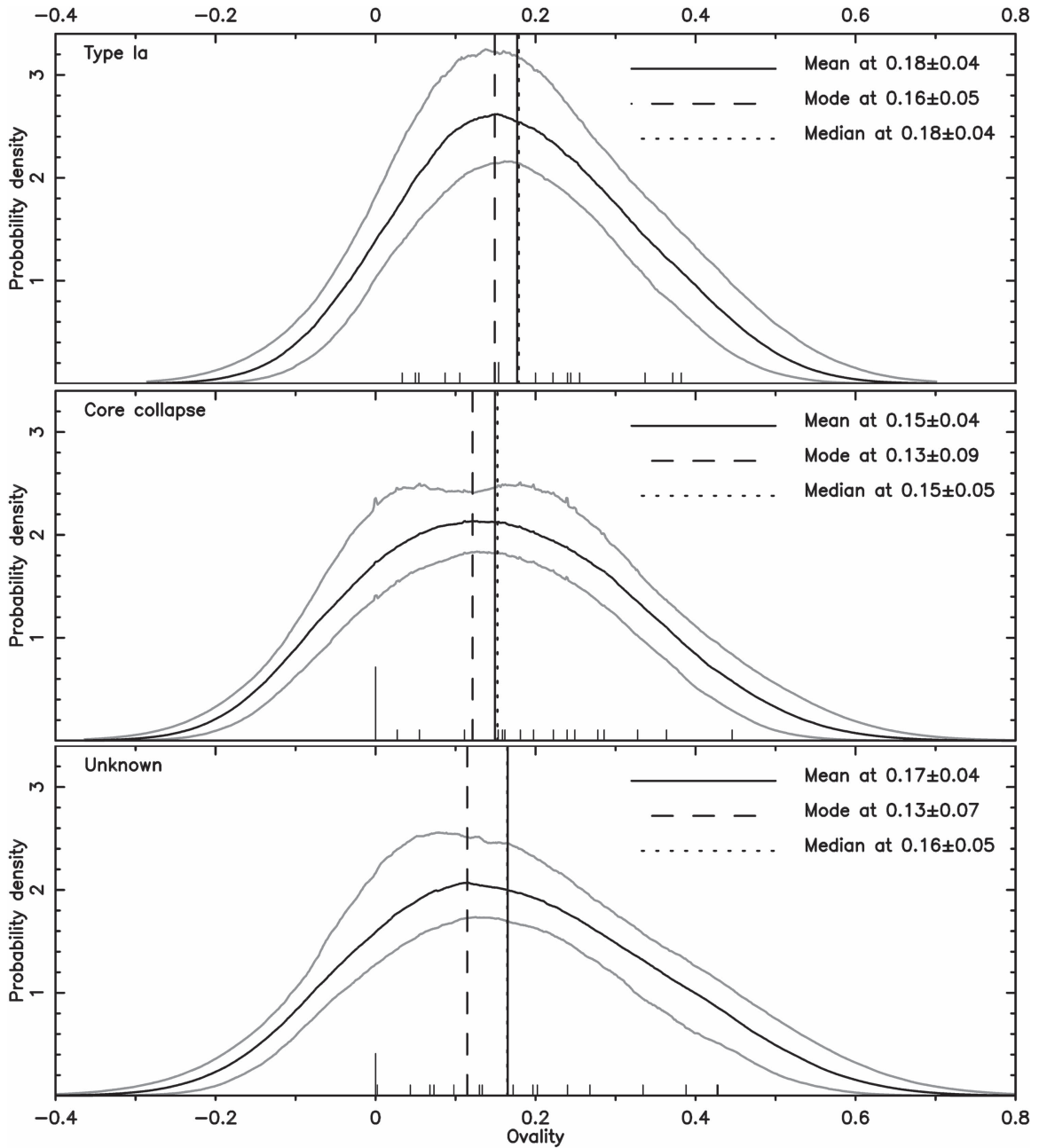


Figure 10. Smoothed density distribution for ovality (as in Figure 9), for subsamples based on progenitor type (designated on each panel). The optimal smoothing bandwidths for the analyzed data samples were found to be 0.107, 0.112, and 0.124 for type Ia, CC, and unknown subsamples, respectively.

Table 3
Results of the Anderson–Darling Two-sample Test

S1 versus S2	n	m	A_{nm}^2	$A_{nm}^2 / \alpha = 0.1$
Unknown versus type Ia	20	16	1.150	1.933
Unknown versus CC	20	23	0.331	1.933
Type Ia versus CC	16	23	1.556	1.933

Note. The comparison samples (S1 and S2) are given in the first column while the rest of the columns present the number of objects in S1, number of objects in S2, calculated value of the Anderson–Darling variable for the two-sample test (A_{nm}^2), and value for the specific confidence level α (A_{nm}^2 / α) at $\alpha = 0.1$ (10%) taken from Pettitt (1976), respectively.

1.0 cm^{-3} , the expected turnover from free expansion to Sedov expansion would fall between $\sim 4.8 \text{ pc}$ and $\sim 31.4 \text{ pc}$. It should be noted, however, that a progenitor star’s mass may exceed the given $40 M_{\odot}$ (Gal-Yam et al. 2009), and that densities can vary significantly (e.g., cold atomic regions of the ISM have densities of $20\text{--}50 \text{ cm}^{-3}$, while molecular regions may be as high as $10^2\text{--}10^6 \text{ cm}^{-3}$ (Ferrière 2001 and references therein). Therefore, such cutoff levels are far from being well-established. The upper limit of Sedov expansion (i.e., the turnover to snowplow evolution) is estimated by Woltjer (1972) to be 50 kyr, or $D \sim 48 \text{ pc}$. These estimated turnover diameters are in moderate agreement with Berkhuijsen (1987),

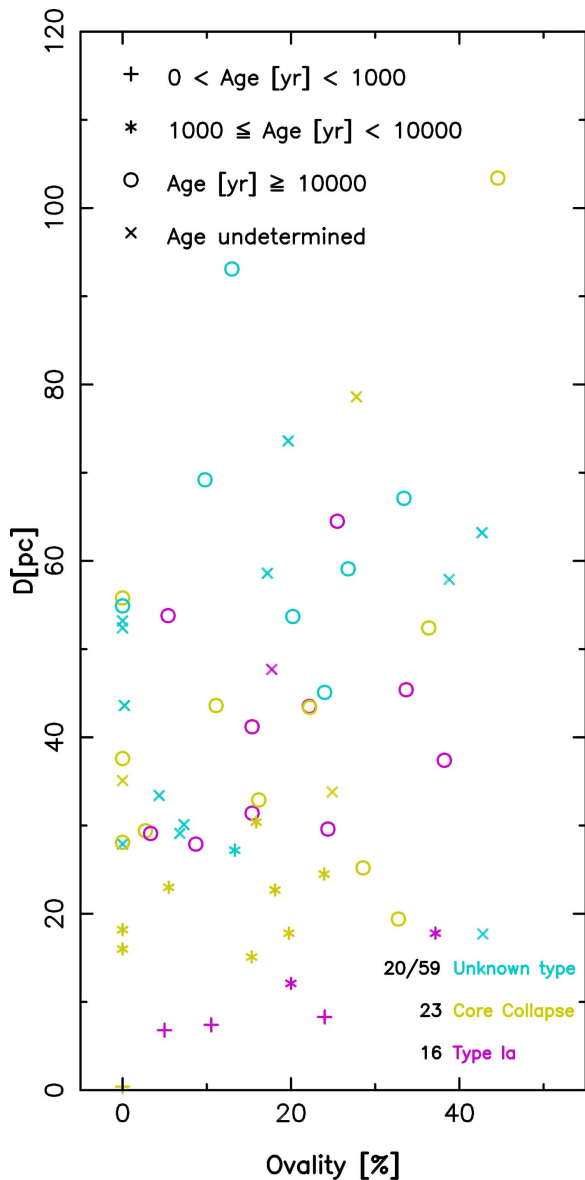


Figure 11. Geometric mean diameter vs. ovality (%) graph. Also, we plot the SNR age and the SN explosion type where known. No correlation was found between any of these LMC SNR parameters. The measurement uncertainties are significantly smaller than the data scatter, and the main reason for the data scatter is likely to come from oversimplifying the model since it is likely that plotted variables are much more dependent on other parameters (e.g., ambient medium properties, explosion energy, ejecta mass, etc.).

who found evidence that SNRs are radiative between $D_R(n_0 = 1) \simeq 20$ pc to 40 pc.

If we assume that the expansion is in the form of a power law $D \propto t^m$, then $N(<D) \propto D^a$, where $a = 1/m$. This means that for the free expansion, $a \simeq 1$ is expected, while in the Sedov phase, the slope in log–log space would be $a = 2.5$.

Early studies of the $N(<D)$ relation for SNRs in the Galaxy and the LMC found exponents of ≈ 1 (Mathewson et al. 1983; Mills 1983; Mills & Turtle 1984), implying that the majority of the remnants are in free expansion. However, Berkhuijsen (1987) made the point that such an exponent is readily mimicked by any influence tending to randomize diameters. Later studies by Long et al. (1990), Smith et al. (1993), and Gordon et al. (1998) found steeper slopes, common to later phases such as Sedov or snowplow expansion. For example, in

their study of SNRs in M33, Gordon et al. (1998) found an $N(<D)$ relation consistent with Sedov expansion and inconsistent with free expansion, inferring that if the ISM is similar to our own Galaxy and the LMC, then these galaxy surveys are seriously incomplete. In their study of SNRs in M83, Dopita et al. (2010) found a slope consistent with free expansion for nuclear remnants, whereas remnants residing in the disk generally followed the expected value of the radiative phase ($N(<D) \propto D^{7/2}$). In M31, Lee & Lee (2014) found two breaking points in the data: one at 17 pc and another at 50 pc. The first component (SNRs with $D < 17$ pc) showed a power-law slope of $a = 1.65 \pm 0.02$, while the second component ($17 \text{ pc} < D < 50$ pc) was in line with Sedov expansion, with a slope of $a = 2.53 \pm 0.04$.

Here, we make distinctions between the types of SNRs based on their morphologies. Lee & Lee (2014) defined so-called A-type remnants as those with well-defined shells. The slope for this subclass of M31 SNRs was found to be $a = 2.15 \pm 0.09$ for $25 \text{ pc} < D < 45$ pc. In their study of M33, Gordon et al. (1998), using a maximum likelihood estimate fit to the $N(<D)$ relation, found slopes for $D_{\text{max}} = 30$ pc and $D_{\text{min}} = 8$ pc and 10 pc of $a = 2.2 \pm 0.05$ and $a = 2.3 \pm 0.06$, respectively, while $D_{\text{max}} = 35$ pc and $D_{\text{min}} = 8, 10,$ and 15 pc showed slopes of $a = 2.0 \pm 0.04$, $a = 2.0 \pm 0.05$, and $a = 1.1 \pm 0.06$, respectively. For the SMC, Filipović et al. (2005) found an overall slope for the galaxy of $a = 1.7 \pm 0.2$.

In Figure 12, we present our results for the LMC. The top of Figure 12 shows cumulative counts versus diameter for all 59 confirmed LMC SNRs in log–log scale. The red line shows the best fit with a slope $a = 1/m = 0.96$. Since the sample above $D > 40$ pc seems to be somewhat incomplete, only the first part of the curve was fitted (for an alternative view, see, e.g., Badenes et al. 2010). The population exponent $a = 0.96$ is close to 1, even given the larger population and more complete sample size of this study. Therefore, the earlier suggestion by Berkhuijsen (1987) regarding randomized diameters readily mimicking such an exponent is probably the case in our LMC sample, and not that the relation is indicative of the SNR population in the galaxy to be in free expansion. The exponent $1 < a < 2.5$ may also indicate that the population is somewhere between free expansion and the Sedov phase. Although this is unlikely in the case of the LMC sample, we have used a simple model for the SNRs’ expansion velocity (Arbutina 2005; Finke & Dermer 2012),

$$\frac{1}{2}v^2 = \frac{k_1 E_o}{k_2 M_E + 4\pi R^3 \rho_o / 3}, \quad v = \frac{dR}{dt}, \quad (13)$$

and combined it with $dN/dD = 1/(2\tau v)$ in order to perform a non-linear fit to the data (again, only the first part of the curve was fitted). In Equation (13), E_o is the explosion energy, M_E mass of the ejecta, and ρ_o is the ISM density. The constants k_1 and k_2 are determined in such a way that when $E_o = 1$ foe¹² and $M_E = 1.4 M_\odot$, $v \approx 20,000$ km s^{−1}, and when $R \gg R_{\text{pc}}$, the velocity tends toward the Sedov solution. In Figure 12 (bottom) we show the differential distribution for the number of LMC SNRs versus diameter. The red curve represents the best-fit model obtained by applying Equation (13), which is still far from good. For a fixed energy of 1 foe and $M_E \sim 10 M_\odot$ (although the sample could contain few SNe Ia), the fit gives a

¹² Energy unit; 1 foe = 10^{51} erg.

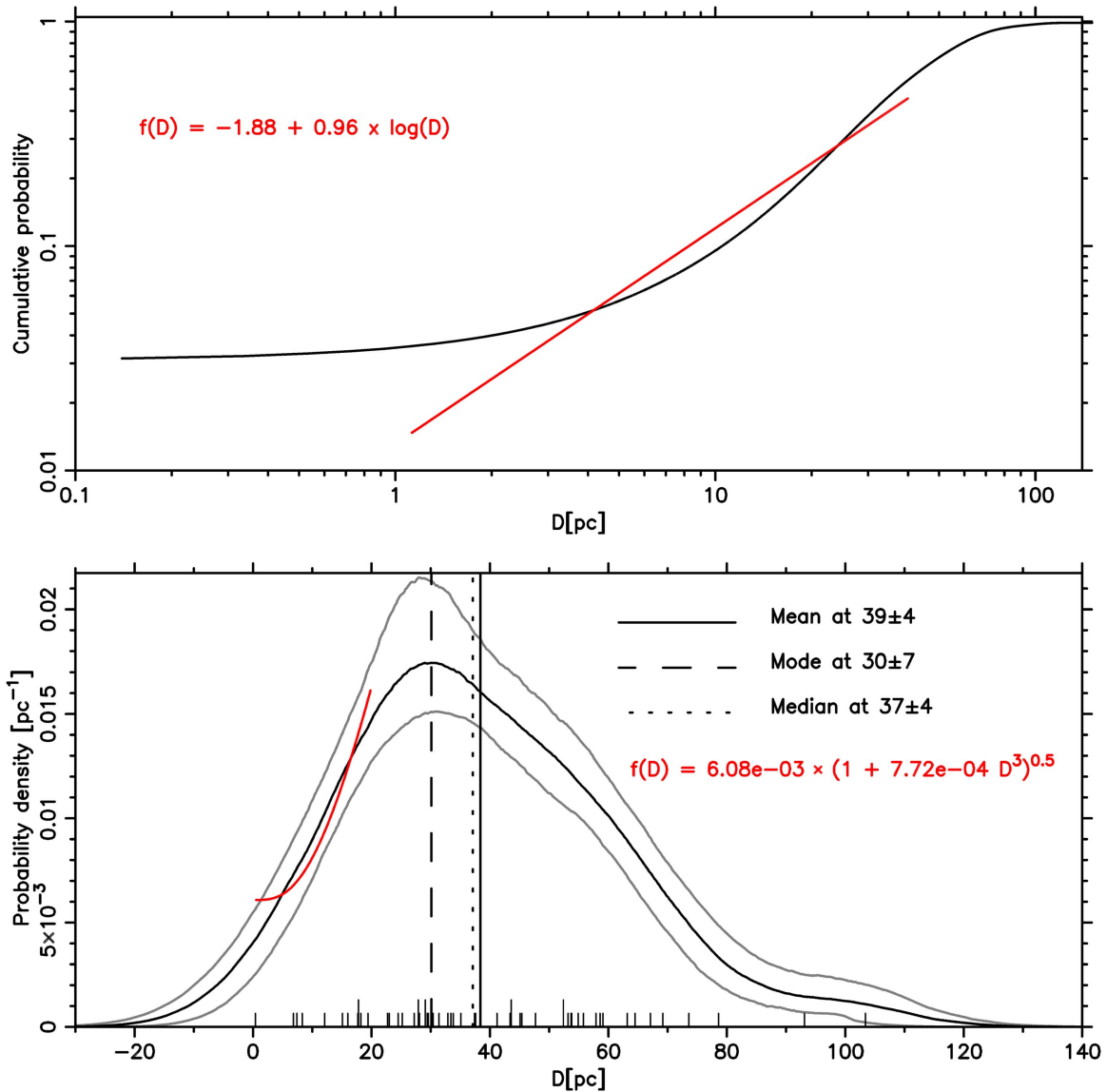


Figure 12. Top: cumulative (integrated) probability distribution from the bottom panel presented on a log–log scale. The red colored lines are the best fit lines to the plotted distributions, from approximately 1 to 40 pc (top), i.e., from the data point with the smallest diameter to the diameter value at the estimated inflexion point at ≈ 20 pc (bottom). Bottom: distribution from the bottom panel of Figure 8.

supernova¹³ rate of 0.55/cy (twice as high as rates found in the literature, e.g., 0.23/cy; van den Bergh & Tammann 1991), while the density is quite low, $\sim 0.03 \text{ cm}^{-3}$, which is not surprising for SNRs still close to the free-expansion phase. As explained above, this density is unrealistically low.

6. Spectral Indices and Evolution in Radio Continuum

Following Gordon et al. (1998), the radio spectral index (α) of an SNR is a measure of the energy distribution of the relativistic electrons producing synchrotron radiation. Assuming a power law for the injection spectrum of relativistic particles of the form

$$N(E) \propto E^{-\gamma}, \quad (14)$$

where E is the energy of the relativistic particle and γ is the power-law index of the energy spectrum, the radio spectral

index is related via

$$\alpha = -\frac{\gamma - 1}{2}. \quad (15)$$

From Bell (1978b), it is seen that diffusive shock acceleration (DSA) can accelerate relativistic particles in a remnant, such that

$$\gamma = \frac{\chi + 2}{\chi - 1}, \quad (16)$$

where χ is the compression ratio in the shock front. In ideal monatomic gas, the limiting compression ratio is 4, resulting in a power-law index of 2, and thus, a spectral index of -0.5 .

6.1. Radio-continuum Spectral Index Distribution

The mean spectral index of the reconstructed distribution is $\alpha = -0.52 \pm 0.03$ (with sample SD = 0.13), calculated from the 41 LMC SNRs where a reliable spectral energy distribution could be estimated. Individual remnant indices as well as

¹³ cy is centi-year or century.

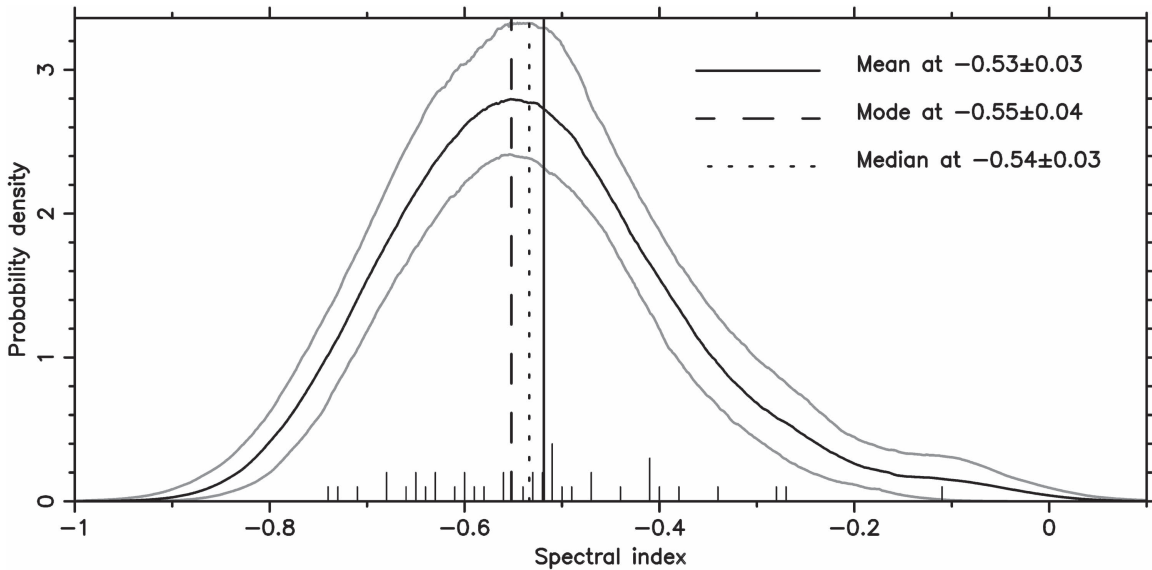


Figure 13. Spectral index smoothed density distribution (as explained in Section 4) for the sample of 41 LMC SNRs with round-up values for mean, mode, and median. We used a 75% confidence interval for estimating the uncertainties (gray lines). We note that a number of SNRs have an overlapping spectral index value, even though they were estimated to an accuracy of two decimal digits (see also Table 1). The data points are marked with vertical dashes on the horizontal axis, with dash length proportional to the number of SNRs in the sample with the corresponding spectral index value. Younger SNRs are generally found toward the steeper indices, while older remnants tend toward the flatter end of the distribution (physical explanations for why this is believed to occur are discussed in Section 6.2). The optimal smoothing bandwidth for the analyzed data sample was found to be 0.077.

associated properties can be found in Table 1, while a reconstructed differential distribution (similar to the reconstructed distributions from Figure 8) of these values can be seen in Figure 13. The mean value of -0.52 is in line with the theoretically expected spectral index of $\alpha = -0.5$ (as discussed above). The left side of the distribution is predominately composed of young SNRs, while older remnants or those harboring a pulsar are found toward the right end of the PDF.

Comparing to other galaxies, Filipović et al. (2005) found a mean spectral index of -0.63 ($SD = 0.43$) for confirmed and candidate SNRs in the SMC. In the MW, Clark & Caswell (1976) found a mean spectral index of -0.45 with an SD of ~ 0.15 .

6.2. Radio-continuum Spectral Index Evolution

To investigate the relationship between a remnant’s age and its radio spectral index, we plotted these two properties against each other (Figure 14; top), resulting in a power-law fit for the 29 SNRs with an established age in the LMC:

$$\alpha = -0.97 \pm 0.09 \times t_{\text{yr}}^{-0.06 \pm 0.02}, \quad (17)$$

where t_{yr} represents the remnant’s age in years. The fit parameter values are calculated as mean values from an array of 10^3 values for each parameter obtained by fitting (non-weighted fit) the resamples of the original data sample (for more details on the bootstrap procedure, see Efron & Tibshirani 1993). The parameter uncertainties are calculated as standard deviations of the corresponding arrays. Some of the earlier studies (e.g., Clark & Caswell 1976) indicated that a remnant’s spectral index did not appear to be correlated with any other parameters. However, this conclusion was generally formed when smaller samples of remnants were available or used. In our study, we found the trend that younger remnants exhibit significantly steeper spectral indices, while mid-to-older

remnants show flatter indices. Also, we found that the average spectral index for this sample of 29 LMC SNRs with known age (and spectral index) is $\alpha = -0.55$, which is fractionally steeper than that for the whole sample ($\alpha = -0.52$). It is likely that this is because it is easier to obtain an age for younger, and therefore brighter, SNRs, which have steeper spectral indices.

The notion that older SNRs exhibit flatter indices was first recognized by Harris (1962) based on observational evidence. Onić (2013) and Urošević (2014) suggested that SNR dimming may be explained by the contribution of the second-order Fermi mechanism, higher shock compressions, or/and thermal bremsstrahlung. Conversely, the steeper spectra found for younger SNRs may be explained by optically thin synchrotron emission produced from accelerated electrons and compressed magnetic field produced at the shock front (Staveley-Smith et al. 2005). Further, Bell et al. (2011) suggested that expansion into a Parker spiral may produce a geometry favoring quasi-perpendicular shocks and spectral steepening.

One should also not forget that there is evidence that the SNR radio spectral index significantly flattens when the SNR shell interacts with surrounding molecular clouds (Ingallinera et al. 2014). The linear fits in Figure 14 are not likely to capture all of the features of the data as we do not know precisely what causes the spread. It could be a wide variety of factors spanning from the excess in N_{H} , differing supernova energies and types, to differing number densities.

To compare our results with those from other galaxies, we re-plotted all values in Figure 14 (bottom) alongside spectral index and age data from SNRs in the MW (Green 2014) and SMC (Filipović et al. 2005, 2008). As can be seen, there is a good alignment between the galaxies. SNR ages, except for the few historical SNe, are derived assuming a hydrodynamical model, usually Sedov, linking age $t \propto R/v_s$. The shock speed v_s is derived from X-ray fitting ($\propto \sqrt{kT}$) and is independent of

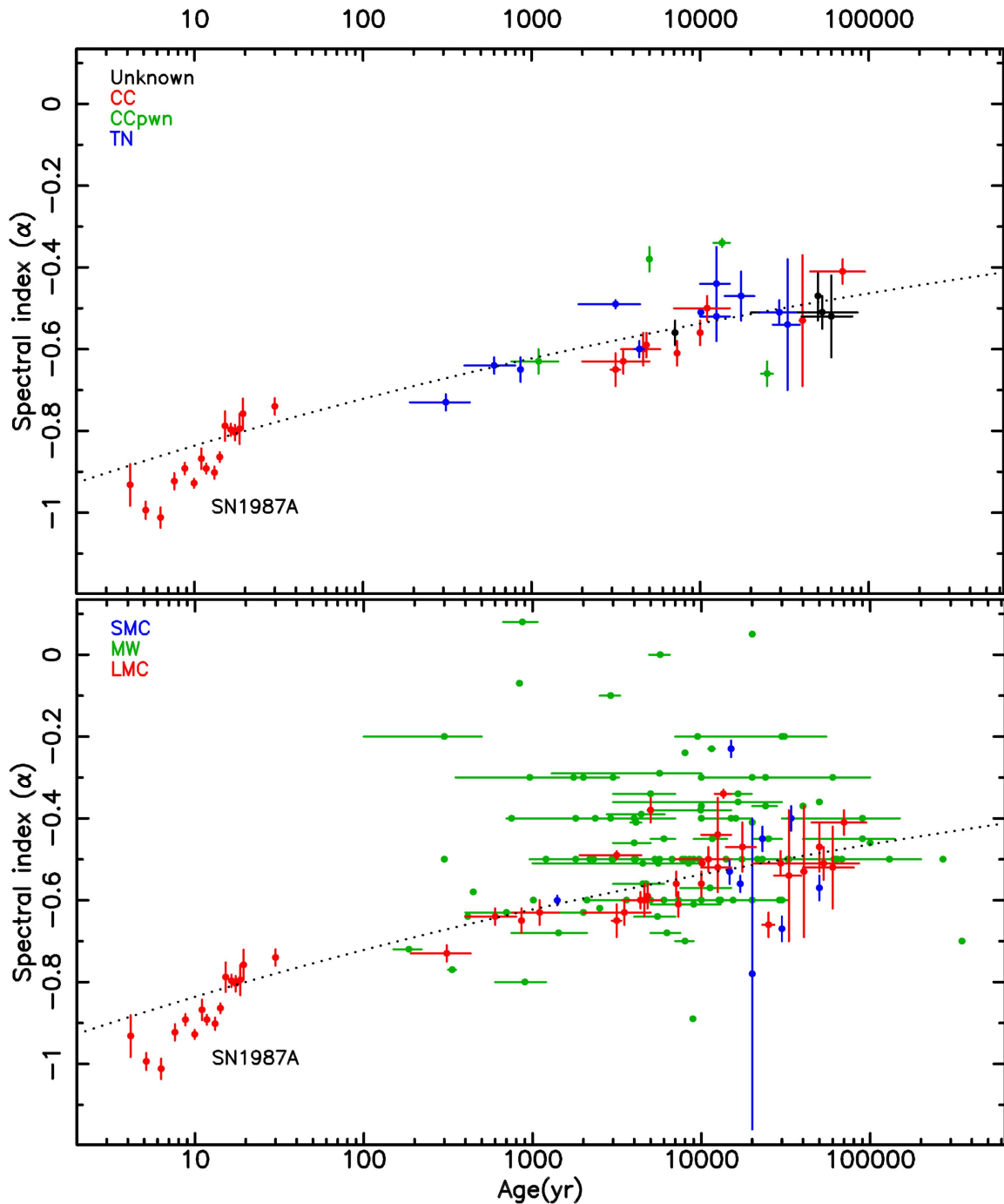


Figure 14. Top: radio spectral index vs. age for the LMC SNR sample of 29 remnants with known ages and spectral indices. The data points located toward the left of the plot are all from SN 1987A (data from Zanardo et al. 2010; Ng et al. 2013; Callingham et al. 2016), representing the data from earlier times; however, only the most recent (2016) is included in the population fit. The black dashed line shows a power-law fit to the 29 SNRs, resulting in $\alpha = (-0.97 \pm 0.09) \times t^{-0.06 \pm 0.02}$. Bottom: same as the top with the addition of the SMC and MW samples.

distance (D), so $t \propto R(kT)^{-1/2} \sim \theta D(kT)^{-1/2}$, where θ is the observed angular diameter. Thus, distance uncertainties contribute most of the uncertainty in age measurements. As noted in Section 1, D is most poorly known for Galactic objects, leading to large age error bars. However, for the LMC objects, a common distance of 50 kpc is assumed so the age measurement does not suffer from such large uncertainties.

In a similar fashion to the age–spectral index relation, a diameter–spectral index relation was created, which gives a

better view of the entire sample of remnants, resulting in

$$\alpha = (-0.8 \pm 0.1) \times D_{\text{pc}}^{-0.12 \pm 0.03}. \quad (18)$$

As expected from Figure 14, smaller (which would generally imply younger) remnants tend to exhibit steeper spectral indices, while their larger counterparts show flatter indices. Similarly to the age–spectral index relation, we compare these results with those from the SMC and MW sample (see

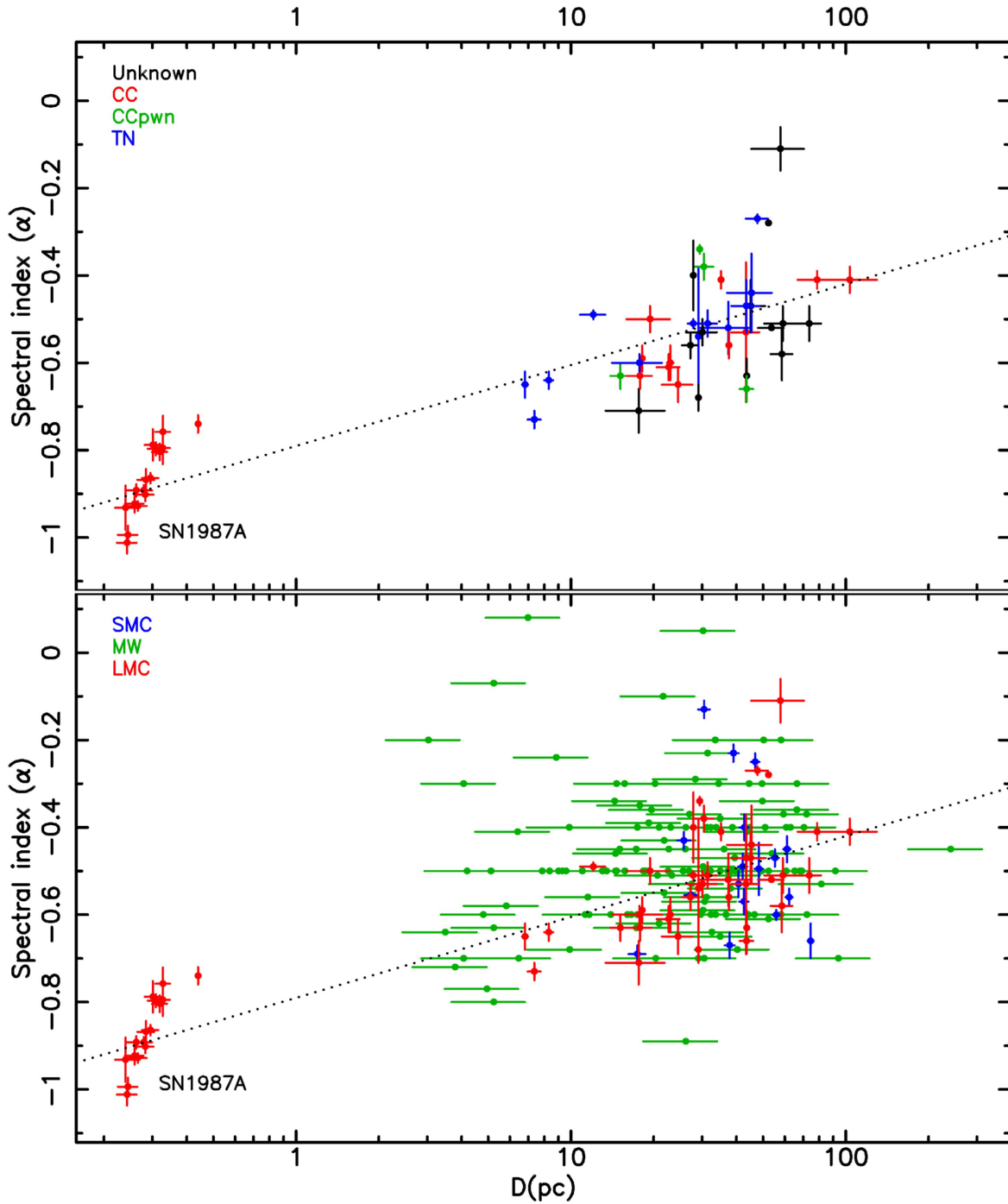


Figure 15. Top: radio spectral index vs. diameter for the sample of 41 LMC SNRs with measured spectral indices. The data points located toward the lower-left corner of the plot are all from SN 1987A, representing the data from earlier times. However, they are not included in the fit. A fit to the measurements (using only the latest data point for SN 1987A (from Callingham et al. 2016)) results in $P = 0.18 \pm 0.04$, $\alpha_0 = -0.79 \pm 0.07$ from Equation (19). Bottom: same as the top, with the addition of data from remnants in the SMC and MW.

Figure 15, bottom). There is a loose alignment in the results, although remnants in the MW generally appear to exhibit flatter indices at the same diameter compared to the LMC sample.

Glushak (1985) studied the evolution of young shell SNRs using eight Galactic remnants, in addition to the one located in the LMC. He found that the remnants' spectral indices flattened as they got larger and older, in line with the results in this study. Glushak (1996) used positive α -values expressed in the

form

$$\alpha = P \log\left(\frac{D_{\text{pc}}}{\text{pc}}\right) + \alpha_0 \quad (19)$$

to find values of $P = -0.58 \pm 0.07$, $\alpha_0 = 0.62 \pm 0.03$ for M82 and NGC 253 ($0.3 < D < 4$ pc), and $P = -0.54 \pm 0.03$, $\alpha_0 = 1.03 \pm 0.02$ for the Galaxy and M31 ($3 <$

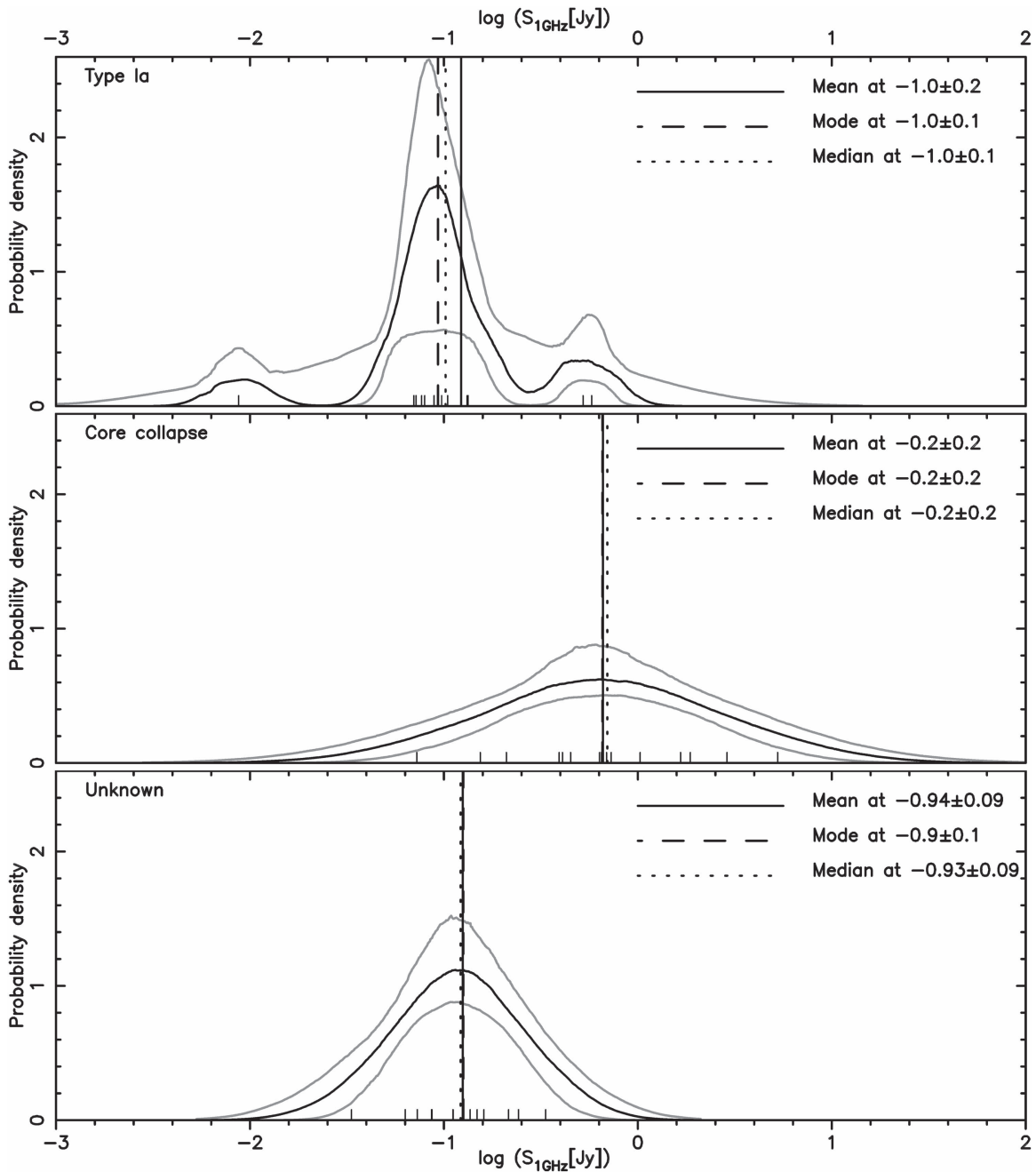


Figure 16. Smoothed density distribution for 1 GHz flux density data (as in Figure 17), for subsamples based on progenitor type (designated on each panel). The optimal smoothing bandwidths for the analyzed data samples were found to be 0.369, 0.458, and 0.265 for type Ia, CC, and Unknown subsamples, respectively. Unlike the distribution in Figure 17, these were smoothed on the $\log S_{1\text{GHz}}$ scale.

$D \leq 21$ pc). He concluded that young shell SNRs evolve differently in galaxies with and without starbursts. Using the same method for the sample of LMC SNRs listed in Table 1, we found $P = 0.18 \pm 0.04$, $\alpha_0 = -0.79 \pm 0.07$ (see Figure 15; bottom), which shows that the spectral index flattening is much less severe as the remnant evolves, in line with the age–spectral index relation.

6.3. Flux Density Distribution

Similar to the SNR spherical symmetry tests (Section 5.4), the independence of the flux density subsamples presented in Figure 16 was tested with the Anderson–Darling two-sample

test. For the CC versus type Ia SNRs, the Anderson–Darling variable test value is 6.4, which is significantly higher than 3.857 (a critical value for 0.01 level from Pettitt 1976), indicating (with a probability of >99%) that CC and type Ia remnants belong to vastly separate populations of objects. Similar results are found for CC versus Unknown SN type with even higher confidence since the value of the Anderson–Darling variable is 7.2. This implies that SNRs with an undetermined progenitor type are more likely to originate from type Ia than CC progenitors. This is in agreement with the remaining case (type Ia versus Unknown) where the Anderson–Darling variable is 0.73, which is well below 1.933 (a critical value at 0.1 level value as also used in Table 3 for testing ovality based subsamples), indicating that the

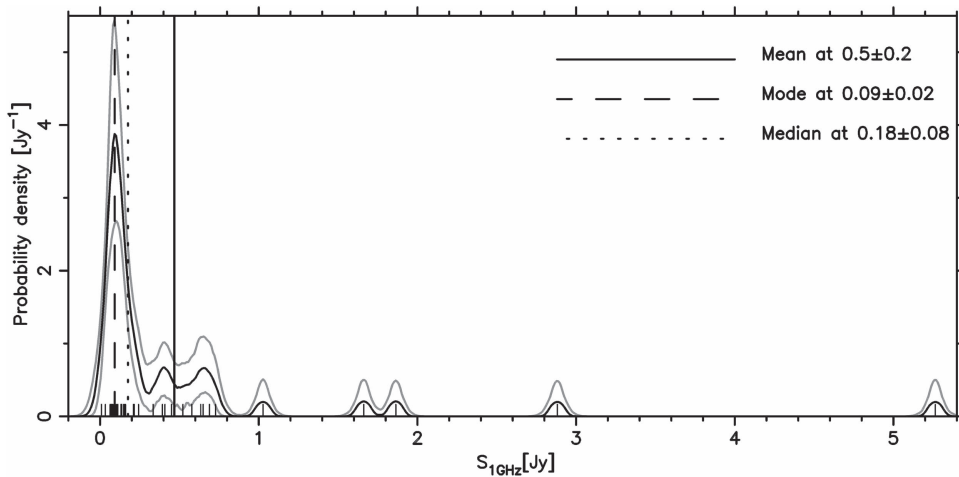


Figure 17. 1 GHz flux density smoothed density distribution (Section 4) for the sample of 40 LMC SNRs with measured flux densities. The round-up values for the mean, mode, and median are also presented. The data points are marked with vertical dashes on the horizontal axis. Distribution parts with $S_{1\text{GHz}} < 0$ have no physical meaning and are plotted for completeness. A confidence interval of 75% was used for estimating the uncertainties (gray lines). The optimal smoothing bandwidth for the analyzed data sample was calculated to be 0.0491 Jy.

tested samples are likely sampled from the same underlying distribution. We also emphasize that the second youngest (310 yr old; Bozzetto et al. 2014a; Hovey et al. 2015) SNR in the LMC—MCSNR J0509-6731—is a well-known type Ia and a relatively weak radio emitter with $S_{1\text{GHz}}$ of 97.4 mJy.

The flux density distribution for the 40 LMC SNRs that have estimated flux densities are shown in Figures 16 and 17.¹⁴ The flux density variable is, by its own nature, heavily biased with sensitivity selection. The faint objects are not usually detected in surveys alongside the majority of the objects but rather with specialized high sensitivity observations. This is reflected in the fact that only $\sim 70\%$ (40 out of 59) of known LMC SNRs have radio flux density measurements. When candidate SNRs are added, this number remains similar— $\sim 67\%$ (49 out of 74). The object DEM L71, which has the lowest flux value, is a well-observed and studied object, unlike much of the sample (see also Section 6.4). Compared with other objects in the vicinity of the PDF mode (which is close to DEM L71), this object and its immediate neighbor [HP99] 460 appear to be rather well-separated. This implies that the highest concentration of detected objects is very close to the sensitivity limits of the related observations and that surveys with sensitivities below 50 mJy should give a large number of new detections.

Although there are known LMC SNRs with 1 GHz flux densities less than 50 mJy, most of the sub-50 mJy sample is lacking reliable flux density estimates. This is because of confusion due to unassociated nearby emission, e.g., an H II region or a nearby and strong background source. Also, some of the remnants are lacking flux density estimates because they are either too weak to be accurately measured or fall below the detection limit of the present generation of surveys. Future radio telescopes (such as Australia Square Kilometre Array Pathfinder, ASKAP) with higher sensitivity and resolution will be able to account for these remnants and provide a more complete sample.

¹⁴ SNR 1987A is excluded from the analysis because of its separation from the rest of the sample and different physical characteristics.

6.4. Radio to X-Ray Flux Density Comparison

We compared our estimated radio flux densities at 1 GHz (Table 1) and broadband X-ray flux in the 0.3–8 keV range from Maggi et al. (2016). There are 58 known LMC SNRs with X-ray flux and/or radio flux density measurements (see Figure 18). Only one confirmed LMC SNR (J0521-6542) has no measurements at either frequency.

At present, the SNR with the faintest measured radio flux density is DEM L71. As it is a well-studied SNR (and one of the brightest X-ray SNRs in the LMC), there are many deep radio observations available for DEM L71 that make its detection and radio flux density measurement easier than for most of the LMC sample. The color-coded symbols in Figure 18 at ~ 6 mJy, indicating radio non-detections, are not representative of true flux density limits. While the rms noise will vary significantly across the LMC, the average radio sensitivity limit for the non-detected sample is > 10 mJy. Likewise, the three X-ray non-detections (ticks at $\sim 10^{-14}$ erg s $^{-1}$ cm $^{-2}$) stem from a lack of proper coverage (e.g., observations with *XMM-Newton* or *Chandra*), and it is premature to conclude that these sources are intrinsically X-ray fainter.

The two flux-bright sources (N49B and N63A) with $F_{0.3-8\text{keV}} > 1 \times 10^{-11}$ erg s $^{-1}$ cm $^{-2}$ have ages of 3500 and 10,000 years old. The other outlier is N157B (also known as 30 Dor B), which has a bright/young cometary PWN and is 5000 yr old. The total X-ray flux (SNR+PWN, $F_{0.3-8\text{keV}} > 5 \times 10^{-12}$ erg s $^{-1}$ cm $^{-2}$) is given, although the thermal component (SNR only) is only $\sim 2 \times 10^{-13}$ erg s $^{-1}$ cm $^{-2}$ as for the bulk of the sample. The radio flux density for this object (~ 3 Jy) also includes a significant fraction of PWN emission, but is harder to separate as both have a non-thermal spectrum.

It appears that SNRs younger than 10,000 years with higher flux and flux density values in X-rays and radio, respectively, show some correlation between these values. Although it is difficult to quantify, we point to the possible correlation between young type Ia and CC SNRs, though the latter appears somewhat brighter (in both X-rays and radio) than the former. Also, the data points near the plotted 1-1 correspondence line in Figure 18 imply that Type Ia objects might be somewhat younger than CC SNRs. For the 43 objects that have age data (Table 1), the results

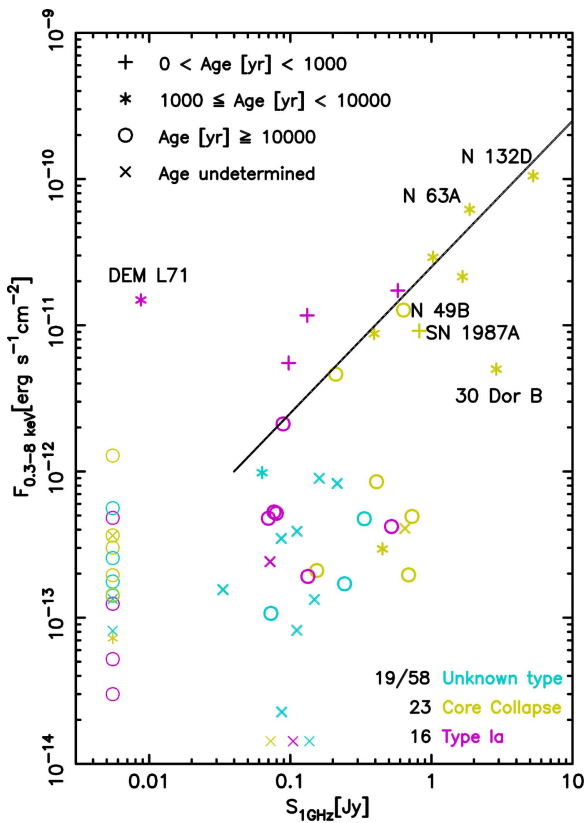


Figure 18. Broadband X-ray flux in the 0.3–8 keV range vs. radio flux density at 1 GHz for 58 LMC SNRs that have estimates for either one or both of these two frequencies. The symbols designate sources that only have estimates for X-ray flux or radio flux density, but not both. The black solid line has the slope of 45° and is plotted to indicate the one-to-one correspondence between the plotted variables for the objects with high values in both frequencies. The position of the thin symbols along the axis with the missing data is offset by a 0.2 log scale from the faintest detection. Four symbols (\times , \circ , $*$ and $+$) indicate SNR age based on Table 1. The pink color symbols indicate type Ia SN events while light green symbols indicate CC SN type. The light blue symbols represent unknown SN types.

of the AD two sample test (see sections 5.4 and 6.3) do not justify the assumption that CC (20 objects) and Type Ia (15 objects) age data subsamples are independent. However, the distribution of objects with an undetermined progenitor type (eight objects) is distinct from the distributions of Type Ia (at $\alpha = 0.05$ level) and CC objects (at $\alpha = 0.1$ level). This is consistent with Figure 18. The objects with undetermined progenitor types, unknown ages, and ages $> 10\,000$ yr have, in general, $F_{0.3-8\text{ keV}} < \times 10^{-12}$ ergs $\text{s}^{-1} \text{cm}^{-2}$. This implies that objects with unknown ages are thus likely to be older remnants that have lost the signatures of their progenitors over time.

There is also a number of radio non-detections that fall into the X-ray flux range of $F_{0.3-8\text{ keV}} < 1 \times 10^{-12}$ erg $\text{s}^{-1} \text{cm}^{-2}$, which confirms the need for more sensitive observations of the LMC SNR population in radio.

6.5. Radio Surface Brightness Evolution

Following the theoretical work done initially by Shklovskii (1960), the important relation connecting the radio surface brightness Σ_ν of a particular SNR at frequency ν and its diameter D can be written in general form as

$$\Sigma_\nu(D) = AD^{-\beta}. \quad (20)$$

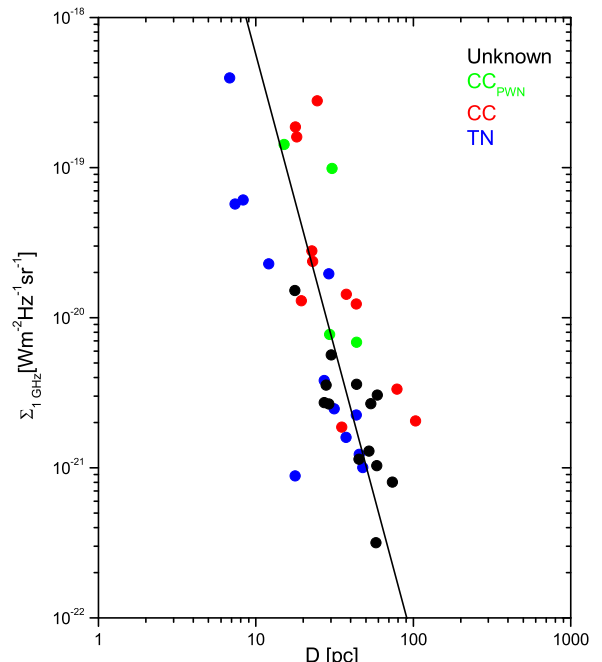


Figure 19. Surface brightness vs. diameter, Σ – D , relation at 1 GHz for LMC SNRs. The solid black line represents the best orthogonal fit ($\beta = 3.92 \pm 1.20$). SNR 1987A, the smallest and brightest SNR in the LMC, is excluded from the graph because of its separation from the rest of the sample and different physical characteristics.

The parameter A depends on the properties of both the SN explosion and the ISM (e.g., SN energy of explosion, ejecta mass, the density of the ISM, the magnetic field strength, etc.), while β is thought to be independent of these properties (Arbutina & Urošević 2005) but explicitly depends on the spectral index α of the integrated radio emission from an SNR (Shklovskii 1960). Parameters A and β are obtained by fitting the data from the sample of SNRs with known distances. Despite all of the criticism of the Σ – D relation (e.g., Green 2005), it remains an important statistical tool in estimating distances to an SNR from its observed, distance-independent, radio surface brightness.

The best-fit correlation (Equation (20)) is a straight line in the $\log D$ – $\log \Sigma$ plane. However, explicit care has to be taken to use the appropriate form of regression. As concluded in Pavlović et al. (2013), the slopes of the empirical Σ – D relation should be determined by using orthogonal regression because of its robust nature and equal statistical treatment of both variables. Both variables suffer from significant scatter and it is not statistically justified to treat one of them as independent. Nevertheless, this is the usual practice, and regressions that minimize over offsets along one variable while the other one is considered as independent, such as $\Sigma = f(D)$ or $D = f(\Sigma)$, are very often used due to their simplicity. In this work we used the more robust orthogonal regression since it minimizes over the orthogonal distance of the data points from the fit line and consequently, both variables have the same significance without one of them being considered the function of the other and measured with infinite accuracy. The orthogonal fitting performs well, regardless of the regression slope for data sets with severe scatters in both coordinates. However, for the extragalactic samples of SNRs, distance (and hence SNR

Table 4
Parameters of Available Nearby Galaxy Data Samples Using Their 5 GHz Radio Fluxes

Name	Number of SNRs	β	$\Delta\beta$	Reference
Entire data sample	214	3.60	0.15	This work
LMC	40	3.78	1.25	This work
SMC	19	5.16	5.76 ^a	Filipović et al. (2005)
M82	31	3.88	0.91	Fenech et al. (2008)
M31	30	2.58	0.68	Urošević et al. (2005)
M33	51	2.66	0.85	Urošević et al. (2005)
Arp 220 ^b	6	Batejat et al. (2011)
NGC 4449, NGC 1569	37	4.68 ^c	2.58	Chomiuk & Wilcots (2009)
NGC 4214, NGC 2366				

Notes.

^a A large bootstrap error for slope β is expected for small samples like the SMC, containing only 19 SNRs.

^b This sample contains only six SNRs and therefore calculating the Σ - D slope does not make physical sense.

^c The Σ - D slope was calculated for the composite sample containing 37 SNRs in four galaxies: NGC 4449, NGC 1569, NGC 4214, and NGC 2366.

diameters) can be obtained with higher accuracy than for the Galactic remnants, since they can be approximated to reside at the distance of the host galaxy. Even in such a case, the depth effect and intrinsic effects can cause significant scatter in D and orthogonal fitting should be preferred.

We can see from extragalactic SNR samples that the intrinsic scatter still dominates the Σ - D relation and errors in distance determination are not crucial, for both Galactic and extragalactic SNRs. Here, the intrinsic scattering originates from the modeling of diverse phenomena with just two parameters (Σ and D) and not taking into account individual characteristics of SNRs such as different SN explosion energies, densities of ISM into which they expand, evolutionary stages, etc. Also, data sets made up of extragalactic SNRs do not suffer from the Malmquist bias because all SNRs are at the same distance, while they still suffer from other selection effects caused by limitations in sensitivity and resolution (Urošević et al. 2005).

For the 40 LMC SNRs with measured flux densities, we estimated the radio surface brightness via

$$\Sigma_\nu = 5.418 \times 10^{-16} \frac{S_\nu}{\theta^2}, \quad (21)$$

where S_ν is the integrated flux density in Jansky (Jy) and θ is the diameter in arcseconds. Our data sample consisting of SNRs from the LMC is displayed in Figure 19, where there appears to be a correlation between Σ and D , in confirmation of the theoretical models. Significant scattering is still present despite having more precise SNR diameters in comparison to the Galactic sample. This is expected due to an intrinsic scatter which dominates any errors arising from the measurement process. Furthermore, SNRs formed from type Ia explosion have lower surface brightnesses than those arising from CC SN events. This is in agreement with the theoretical prediction that the larger ISM density produces greater synchrotron emission from an SNR, given in the form $\Sigma \propto \rho_0^{\eta} \propto n_H^{\eta}$ (Duric & Seaquist 1986; Berezhko & Völk 2004, 2010), where ρ_0 and n_H are the average ambient density and hydrogen number density, respectively. As the distance to the LMC of 50.0 ± 1.3 kpc is determined to a very high accuracy (Pietrzyński et al. 2013), the Σ - D relation is in our case more important from a theoretical point of view, for comparison with Galactic and other extragalactic relations and also for comparing the environments into which SNRs expand.

Surface brightnesses were calculated for the sample of 40 LMC SNRs at 5 GHz and orthogonal fitting was applied. The resulting fit shows a Σ - D slope of $\beta = 3.78 \pm 1.20$, which is very close to the slope $\beta = 3.9 \pm 0.9$ obtained for the sample of 31 compact SNRs from the starburst galaxy M82, at the same frequency (Urošević et al. 2010). The slope errors were calculated by using the bootstrap method. We have done 10^5 bootstrap data resamplings for each fit.

For the purpose of proving the universality of the Σ - D law for SNRs, regardless of which samples are used, we constructed a composite sample containing available extragalactic SNR populations at the same frequency of 5 GHz (214 SNRs in total), which is shown in Figure 21. Properties of the 10 extragalactic samples considered in this paper are listed in Table 4. The entire sample has a compact appearance for the presented variable range, with an overall slope of $\beta = 3.60 \pm 0.15$, very close to that of the LMC sample in this study. The resulting slope indicates that the observed extragalactic SNRs are mainly in the Sedov phase of evolution, as it was predicted by the values of slopes that are theoretically derived (Duric & Seaquist 1986; Berezhko & Völk 2004).

In Figure 22 we show the theoretical “equipartition” models for radio evolution similar to the ones given by Reynolds & Chevalier (1981) and Berezhko & Völk (2004). The emissivity is defined as

$$\epsilon_\nu = c_5 K (B \sin \Theta)^{(\gamma+1)/2} \left(\frac{\nu}{2c_1} \right)^{(1-\gamma)/2}, \quad (22)$$

where c_1 , c_3 and $c_5 = c_3 \Gamma(\frac{3\gamma-1}{12}) \Gamma(\frac{3\gamma+19}{12}) / (\gamma+1)$ are from Pacholczyk (1970). The model assumes $K \propto \epsilon_{CR}$, $\epsilon_{CR} \approx \frac{4}{\gamma+1} \epsilon_B \sim \delta \rho v^2$, $\epsilon_B = \frac{1}{8\pi} B^2$ (Arbutina et al. 2012, 2013), where we applied Equation (13), and assumed a CR proton-to-electron number of 100:1. The slope of Σ - D in the adiabatic phase is then given approximately as $\beta = \frac{-3\alpha+7}{2}$, where α is the spectral index. From Figure 22, we also observe that, as expected, the type Ia events could have overall lower surface brightness and smaller diameters than the known CC population. However, no definite conclusion can be drawn as there are large population of yet unknown SN types.

In addition to dependence on SNR size, the radio surface brightness of an SNR might also depend on the properties of the ambient medium into which the SNR expands. Arbutina & Urošević (2005) argued that based on the progenitor type,

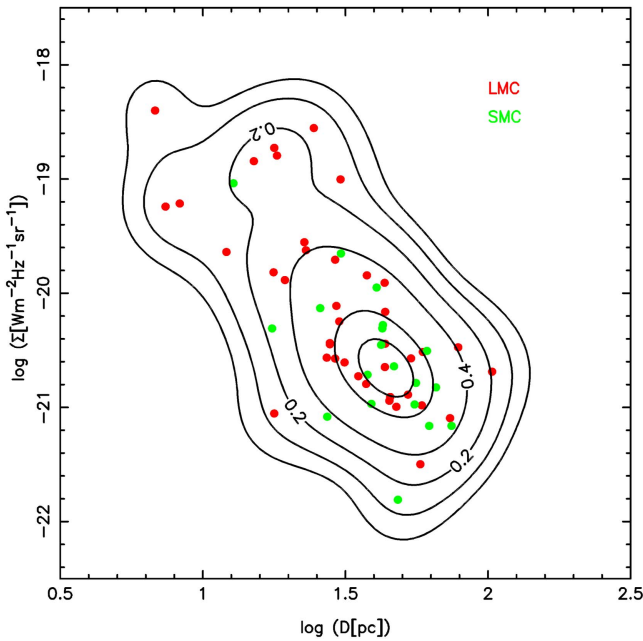


Figure 20. Smoothed density distribution for the sample of LMC and SMC SNRs at 1 GHz, containing 59 SNRs. Red dots represent LMC SNRs while green dots represent SNRs from SMC. Contour levels are at 0.05, 0.1, 0.2, 0.4, 0.8, and 1.0. The procedure for density smoothing is described in Section 4.3 with the relevant parameters given in Section 6.5. As the smallest and brightest object of the sample, SNR 1987A was not considered in this analysis.

SNRs are likely to be associated with an ambient medium of different densities. Consequently, depending on the progenitor type (ambient density), SNRs should form a broad band corresponding to evolutionary tracks in the Σ - D plane. The dependence of Σ - D evolution on ambient density is further explored in Kostić et al. (2016). Under the assumption that SNRs expanding in an ambient medium of higher density have higher Σ , they argued in favor of the dependence of the slope of the Σ - D relation on the fractal properties of the ISM density distribution in the areas crowded with molecular clouds. These clouds are denser than the surrounding ISM and therefore SNRs emit more synchrotron radiation while expanding within it. After reaching the edge of the cloud, SNR evolution continues outside the cloud, and it emits less radiation due to the lower density of the ISM. This effect might result in different slopes of the Σ - D relation.

To further analyze the density dependence, the PDF of the data in the Σ - D plane should be obtained. As described in Vukotić et al. (2014) this has many advantages compared to the standard fit parameter-based analysis since all the information from the data sample is preserved and not just projected onto the parameters of the fit line. We calculated the Σ - D PDF using the kernel density smoothing described in Section 4.3. To test if there are statistically significant data density features in the Σ - D plane, in relation to the $\Sigma(\rho)$ dependence, 2D kernel smoothing was performed on the Σ - D LMC and SMC data sample (containing $40 + 19 = 59$ SNRs; SN 1987A not included in this sample). One hundred smooth bootstrap resamplings were applied in each step of the iterative procedure initialized with $h_0^{\log D} = 0.129$ and $h_0^{\log \Sigma} = 0.389$. The ranges over which the BIMSE was calculated were $h^{\log D} = [0.01, 0.3]$ and $h^{\log \Sigma} = [0.1, 0.7]$, with steps of 0.01 in both dimensions. We obtained optimal smoothing bandwidths at $h^{\log D} = 0.12$ and $h^{\log \Sigma} = 0.34$. The resulting

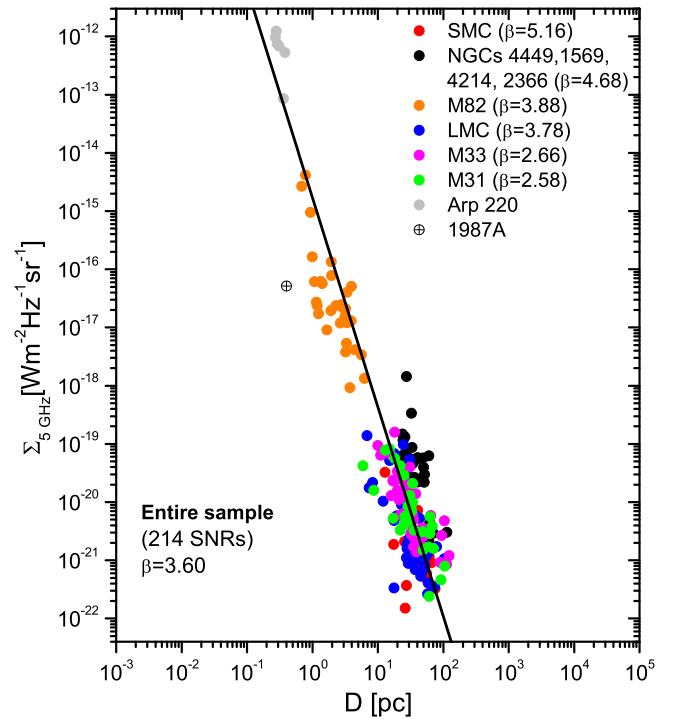


Figure 21. Σ - D graph of LMC SNRs alongside nine other nearby galaxies. This composite sample contains 214 SNRs. Orthogonal fitting has been applied to the 5 GHz data for the galaxies. The youngest known SNR in the LMC, 1987A, is also shown (circled plus), but it is not included in the Σ - D fit, being in the early free-expansion phase of evolution. The solid black line represents the best orthogonal fit to the data ($\beta = 3.60 \pm 0.15$).

$f_{h^{\log D} h^{\log \Sigma}}(\log D, \log \Sigma)$ in Figure 20 was calculated on a regular 100×100 grid mapped on $\log D = (0.5, 2.5)$ and $\log \Sigma = (-22.5, -17.5)$ ranges.

From the given contour plot (Figure 20), it is evident that there are no Σ - D data groupings in parallel tracks that are emergent, or any other features possibly indicative of SNRs expanding out of molecular clouds or outgrowing the relevant density scale of the molecular clouds (as analyzed in Kostić et al. 2016). Further analysis and theoretical work are required on this matter in addition to thorough surveys.

7. Supernova Remnants and Cosmic Rays

Baade & Zwicky (1934) originally proposed that SNRs may be the primary site of CR acceleration. This initiated a debate as to the validity of this claim and to the extent of which SNRs accelerate CRs. Ackermann et al. (2013) measured a gamma-ray spectrum that is better explained by a pion-decay origin rather than a leptonic origin in two galactic SNRs (IC 443 and W44), providing direct evidence that CR protons are accelerated in SNRs. However, CR electrons are similarly important in this debate as they are accelerated in the SNR shock, as revealed by radio synchrotron emission and X-ray synchrotron filaments.

The acceleration of CRs by strong shocks predicts a differential energy power-law spectrum $n(E)dE \propto E^{-\gamma} dE$, with a spectral index of $\gamma = 2$ (Krymskii 1977; Bell 1978a; Blandford & Ostriker 1978). It was suggested that the acceleration of these CRs may be due to them repeatedly crossing the shock in a first-order Fermi process, gaining a fractional energy $\Delta E/E \propto u_s/c$ with each crossover, where u_s is the shock velocity. However, observationally, CR indices are

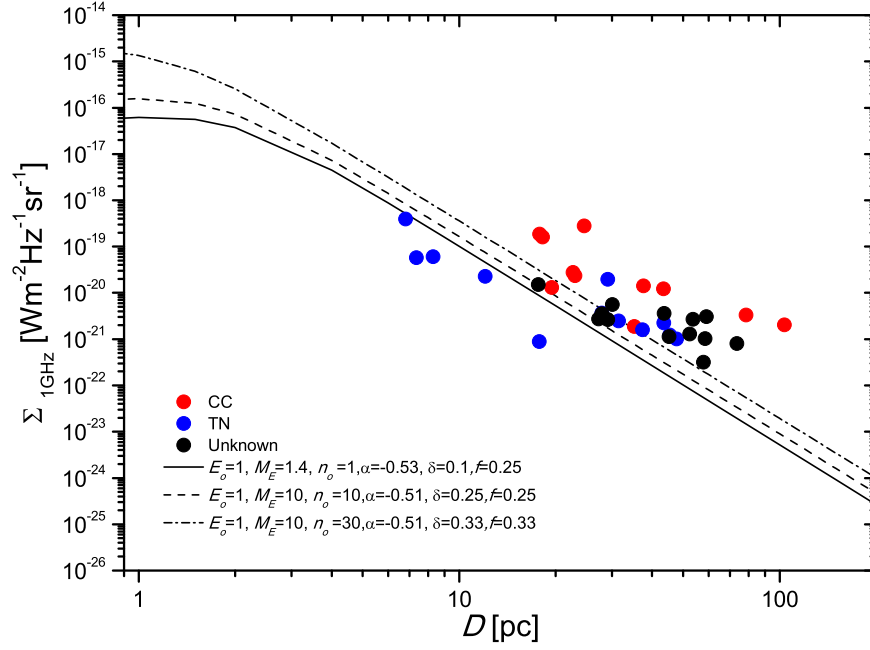


Figure 22. An “equipartition” evolution model $\epsilon_{\text{CR}} \approx \frac{4}{\gamma+1}\epsilon_B \sim \delta\rho v^2$, $\epsilon_B = \frac{1}{8\pi}B^2$, obtained by applying Equation (22), and assuming CR proton to electron number 100:1. Spectral index is α and f is the volume filling factor. The slope is in a range of $\beta = 4.265\text{--}4.295$.

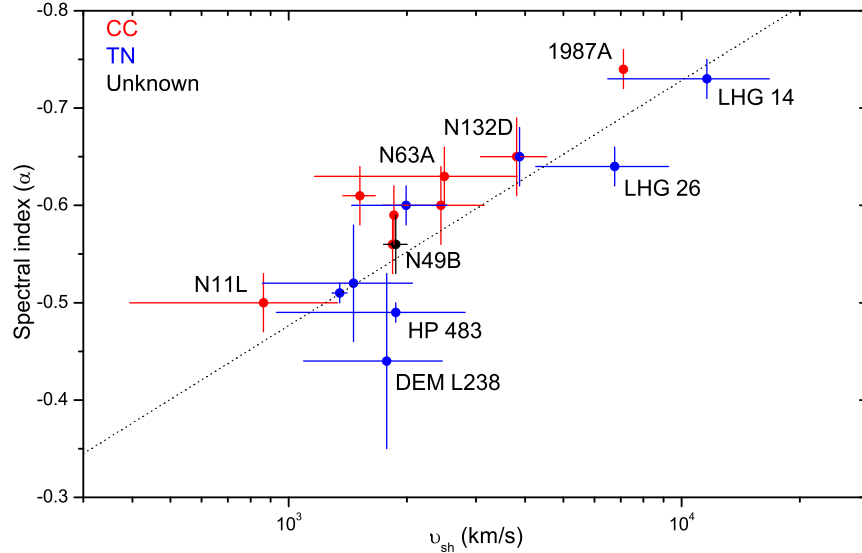


Figure 23. Radio spectral index vs. shock velocity for the sample of 17 young LMC SNRs. These SNRs were selected as they exhibited a clear shell morphology, measured spectral index, and age estimate. The dotted line represents a fit to the entire sample resulting in $\alpha = -0.73 - 0.25 \log_{10}(v_{\text{sh}}/10^4 \text{ km s}^{-1})$.

found to significantly differ from such an index, e.g., the well-known deviation found for relativistic shocks (Kirk & Heavens 1989; Ostrowski 1991; Baring et al. 1993; Achterberg et al. 2001; Kobayakawa et al. 2002). Bell et al. (2011) updated the theory of CR acceleration to explain deviations from $\gamma = 2$ for shock velocities as low as $10,000 \text{ km s}^{-1}$. For this, they plotted the SNR spectral index against its mean shock velocity, that is, the radius of the SNR divided by its age, in lieu of the momentary shock velocity. The reason for taking this approach can be explained to be due to the spectrum being the addition of CRs that have been accelerated throughout the remnant’s lifetime. For their entire sample of SNe and SNRs, Bell et al. (2011) find a trend line of

$$\alpha = -0.7 - 0.3 \log_{10}(v_{\text{sh}}/10^4 \text{ km s}^{-1}), \quad (23)$$

where v_{sh} is the radius divided by the age of the SNRs. For a more reliable set of measurements, they also fit a trend line to only historic SNRs, resulting in

$$\alpha = -0.7 - 0.8 \log_{10}(v_{\text{sh}}/10^4 \text{ km s}^{-1}). \quad (24)$$

Taking the same approach as in Bell et al. (2011), we found:

$$\alpha = -0.73 - 0.25 \log_{10}(v_{\text{sh}}/10^4 \text{ km s}^{-1}), \quad (25)$$

with fit quality $R^2 = 0.86$ (R is the correlation coefficient), for the LMC subsample containing 17 young SNRs with established shell morphology and readily available spectral index and age estimates. We selected only SNRs that are estimated to be younger than 10,000 years. The best fit is represented by the dotted line in Figure 23. This fit is close to the trend line,

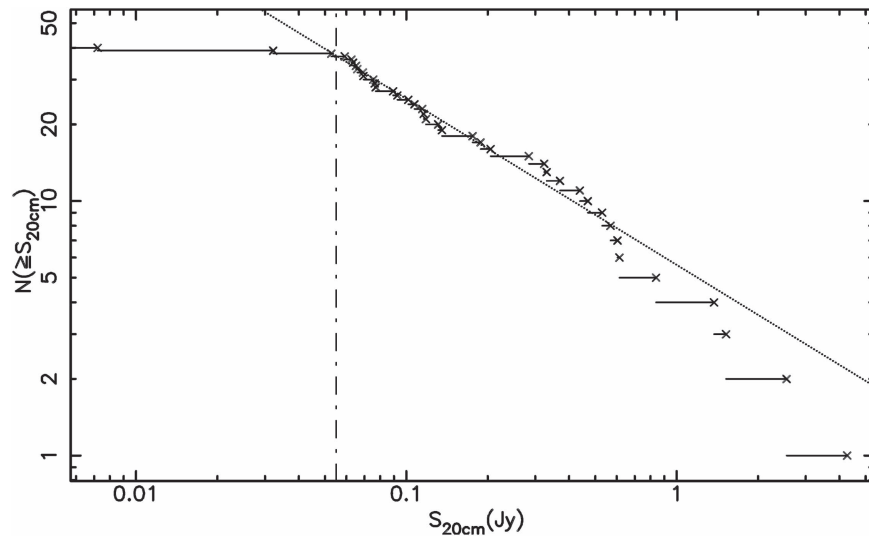


Figure 24. Luminosity function for a sample of 40 LMC SNRs at $\lambda = 20$ cm, represented by a solid line. The dotted line represents the power-law fit to the component above the break at 55 mJy (dashed-dotted line). Crosses mark the data points obtained from the 1 GHz data scaled to 1.4 GHz (20 cm).

described by Equation (23) and found by Bell et al. (2011), for their entire sample of Galactic, historic, and extragalactic SNRs and SNe. Therefore, there appears to be a good alignment with the results between these two studies. Also, the LMC SNR sample confirms that there is a velocity-dependent radio spectral index and that younger SNRs with higher shock velocities seem to have steeper radio spectra.

The luminosity function can be used to test the hypothesis that SNRs are a primary site for CR acceleration. As SNRs only make up a fraction of the synchrotron radiation in the LMC, the electrons produced by SNRs must radiate well after the SNR has dissipated to account for the remaining majority of the synchrotron emission. To investigate this, a luminosity function needs to be created for the LMC SNR sample. To achieve this, we plot the cumulative luminosity function:

$$N(s > S) \propto S^{-b} \quad (26)$$

in Figure 24, using integrated flux densities at 20 cm (deduced from the 1 GHz flux densities and the spectral indices shown in Table 1). As the LMC is located at a distance of ~ 50 kpc, all objects that lie within the galaxy can be treated as approximately equidistant. Therefore, the luminosity and flux density plots will not differ, and they are interchangeable in the text.

It can be seen that the spectrum breaks at ~ 55 mJy, which would imply that the sample is not complete. This was already known, as the sample used here contains only 40 (with SNR 1987A also being excluded from the sample presented in Table 1) out of the 59 confirmed LMC SNRs, or 40 out of the 74 in the total sample including the candidates. Because of this, a simple power-law fit on the whole S range is not appropriate. Therefore, we fitted a power law (with the bootstrap procedure described in Section 6.2) in the $S > 55$ mJy interval (37 data points), resulting in

$$N(\geq S) = (5.6 \pm 0.3) \cdot S^{-0.65 \pm 0.02} \text{ for } 0.055 > S \text{ Jy.} \quad (27)$$

The total integrated flux density for the sample of 40 remnants was ~ 17.5 Jy. In an attempt to account for the missing flux from the SNRs absent from the sample, we used the power-law

Table 5

Fraction of Residency Time of Electrons to SNR Lifetime (τ_e/τ_{snr}) for Different Values of the LMC Magnetic Field and LMC Spectral Index

B_0 (μG)	$\alpha = -0.17$	$\alpha = -0.29$	$\alpha = -0.30$	$\alpha = -0.56$
2	1601	1473	1463	1222
3	996	873	864	649
4	712	603	594	414
5	548	452	445	293

fit from Equation (27) to integrate via

$$\int_0^{4.276 \text{ Jy}} \frac{5.6}{(S)^{0.65}} dS = 26.7 \text{ Jy}, \quad (28)$$

which is a better estimate of the total contribution of non-thermal emission from SNRs in the LMC. As in Duric et al. (1993) we then use the equation

$$\frac{\tau_e}{\tau_{\text{snr}}} = \frac{N_e(\text{LMC})}{N_e \text{ SNR}} = \frac{S_{20}(\text{LMC}) B_0(\text{SNR})^{1-\alpha(\text{SNR})}}{S_{20}(\text{SNR}) B_0(\text{LMC})^{1-\alpha(\text{LMC})}}, \quad (29)$$

where τ_e represents the residency time of electrons in the disk of the galaxy, τ_{snr} is the lifetime of the remnant, and S_{20} is the non-thermal flux density at 20 cm. The equation has a similar form to that in Duric et al. (1993) with the sign of α being the only difference. Duric et al. (1993) used $S \propto \nu^{-\alpha}$ while here we adopted the $S \propto \nu^\alpha$ form.

Along with the estimate of the total contribution of flux density from SNRs from Equation (28), we substituted the non-thermal flux density of the LMC at 20 cm given by Hughes et al. (2007), who stated that the LMC exhibits a radio flux density of 426 Jy, where $\geq 20\%$ is thermal origin.¹⁵ The magnetic field strength of the LMC was taken to be $B_0 \approx 1 \mu\text{G}$ (Gaensler et al. 2005) and a typical SNR would exhibit $B_0(\text{SNR}) = 40 \mu\text{G}$ (Arbutina et al. 2012, 2013) and $\alpha = -0.52$ (Figure 13). The spectral index of the LMC is difficult to constrain, and in the literature we found a range of

¹⁵ We note here that radio flux from some SNRs might also have a significant thermal component (Urošević 2014; Onić 2013) but to some degree it is compensated by using the lower limit for the fraction of the thermal radiation of the LMC.

values from -0.29 , -0.17 (Hughes et al. 2007), -0.56 (Klein et al. 1989), and -0.3 (Haynes et al. 1991). We note that the total contribution of SNRs to the non-thermal flux density of the LMC is much higher ($\sim 6\%$) than that found by Gordon et al. (1998) for M33 ($\approx 2\%$ – 3%).

Taking the value of $B_0(\text{LMC})$ to be $1 \mu\text{G}$, the spectral index of the galaxy does not affect the outcome and results in

$$\frac{\tau_e}{\tau_{\text{snr}}} = 3603. \quad (30)$$

If the magnetic field of the LMC is varied, a wider range of values is possible. To investigate this, the τ_e/τ_{snr} values were measured for magnetic field strengths from 2 – $5 \mu\text{G}$ and for spectral index values for the LMC of $\alpha = -0.17$, -0.29 , -0.30 , and -0.56 , which can be found in Table 5.

The measurement of $\alpha(\text{LMC}) = -0.56$ was estimated from a much earlier paper; radio instruments have developed significantly since Klein et al. (1989). If measurements derived from this value of α are omitted, and the average SNR lifetime of $\tau_{\text{snr}} \approx 10^4$ yr is taken, this results in a residency time of 4.4 – 16.0 million years. Although there is a large spread of possible values, this is in line with the residency time of CRs within the Galaxy of 15 ± 1.6 Myr (Lukasiak et al. 1994), and with the value found by the same method for M33 of 7.5 – 10.1 Myr (Gordon et al. 1998). Consequently, these results are in agreement with the hypothesis that SNRs are a predominant source for CR acceleration in the LMC.

8. Conclusions

This work has provided an atlas of the 59 currently confirmed LMC SNRs in addition to 15 candidates from which 7 are shown here for the first time. Our statistical analysis of the available data has led to the following conclusions.

1. Although our LMC sample is the most complete sample of SNRs in any galaxy, the sensitivity detection level is sparse across the different EM domains. This leads to the conclusion that our sample is under the influence of various observational biases. Specifically, the sample with sizes $D > 40$ pc still seems to be incomplete, leaving room for a future detection of mainly large (and older) LMC SNRs (Section 5.2).
2. We found evidence that the 16 known type Ia LMC SNRs are expanding in a somewhat lower density environment (mean = 1.9×10^{21} atoms cm^{-2}) while the 23 known CC type SNRs are expanding in a somewhat denser environment with a mean HI column density of 2.4×10^{21} atoms cm^{-2} . However, the uncertainties are on the larger side, and these suggestions should be taken with caution (Section 5.1).
3. The LMC SNR population exhibits a mean diameter of 39 pc for the confirmed remnants and 41 pc for the combined SNR and SNR candidates sample. These values are comparable to the mean diameters of the M31 (44 pc) and M33 (48 pc) SNR samples (Section 5.3).
4. The spherical symmetry of the LMC SNRs' (or ovality—as defined here) multifrequency emission does not appear to correlate with the type of SN explosion. Also, no evidence for any type of correlation was found between the type of SN explosion, ovality, or its known age (Section 5.4).

5. The $N(<D)$ relationship shows an exponent $a = 0.96$, which is close to $a = 1$, even for the more complete sample given in this paper. Therefore, the earlier suggestion regarding randomized diameters readily mimicking such an exponent is probably the case here and not that the relation is indicative of the SNR population in the galaxy being in free expansion (Section 5.5).
6. The mean spectral index of the LMC SNRs ($\alpha = -0.52$) is in line with that theoretically expected: $\alpha = -0.5$ (Section 6.1). However, our data show a clear flattening of the synchrotron spectral index as the remnant ages (Section 6.2), at a rate of

$$\alpha = 0.18 \log\left(\frac{D}{\text{pc}}\right) - 0.79.$$

7. Radio flux densities from CC and type Ia remnants belong to separate populations of objects. Namely, the CC types are distinctively brighter radio emitters than type Ia remnants. Also, we conclude that the remaining population of presently unknown SNRs might be predominantly populated by type Ia SN explosions (Section 6.3).
8. SNRs younger than 10,000 years with higher flux and flux density values in X-rays and radio, respectively, show good correlation between these values. As expected, the young CC SNRs appear somewhat brighter in both X-ray and radio frequencies than the young type Ia SNRs (Section 6.4).
9. The 5 GHz Σ – D relation for the LMC, with a slope of 3.78, is in line with the average for other nearby galaxies, where a slope of 3.60 was found (Section 6.5).
10. There is a clear relation between the shock velocity of an SNR and its synchrotron spectral index. The trend for velocities of 17 LMC SNRs younger than 10,000 years shows

$$\alpha = -0.73 - 0.25 \log_{10}(v_{\text{sh}}/10^4 \text{ km s}^{-1}),$$

which is in agreement with the slope found for the sample of Galactic and extragalactic SNRs and SNe (Section 7).

11. The radio luminosity function has been used to find a CR electron residency time of 4.4 – 16.0 Myr, which aligns well with the residency time of electrons in the Galaxy, and therefore, consistent with the suggestion that SNRs are the primary site for CRs within a galaxy (Section 7).

We thank the referee (Eric M. Schlegel) for his thorough review and highly appreciate his comments and suggestions, which significantly contributed to improving the quality of our paper. We also thank an anonymous statistical referee whose comments have greatly improved the data analysis and corresponding results of this work. We thank Denis Leahy for discussions and comments. The Australia Telescope Compact Array is part of the Australia Telescope National Facility, which is funded by the Commonwealth of Australia for operation as a National Facility managed by CSIRO. This paper includes archived data obtained through the Australia Telescope Online Archive (<http://atofa.atnf.csiro.au>). D.U., M.Z.P., B.V., and B.A. acknowledge financial support from the Ministry of Education, Science, and Technological Development of the Republic of Serbia through project #176005 “Emission nebulae: structure and evolution.” P.K. acknowledges support from the European

Space Agency PRODEX Programme—Contract Number 420090172. P.M. acknowledges support by the Centre National d'Études Spatiales (CNES). M.S. acknowledges support by the Deutsche Forschungsgemeinschaft through the research grant SA 2131/4-1 and the Heisenberg professor grant SA 2131/5-1. The MCELS was funded through the support of the Dean B. McLaughlin fund at the University of Michigan and through NSF grant 9540747.

Facilities: ATCA, XMM-Newton.

References

- Achterberg, A., Gallant, Y. A., Kirk, J. G., & Guthmann, A. W. 2001, *MNRAS*, **328**, 393
- Ackermann, M., Ajello, M., Allafort, A., et al. 2013, *Sci*, **339**, 807
- Anderson, T. W., & Darling, D. A. 1954, *J. Am. Stat. Assoc.*, **49**, 765
- Arbutina, B. 2005, Master's thesis, Univ. Belgrade
- Arbutina, B., & Urošević, D. 2005, *MNRAS*, **360**, 76
- Arbutina, B., Urošević, D., Andjelić, M. M., Pavlović, M. Z., & Vukotić, B. 2012, *ApJ*, **746**, 79
- Arbutina, B., Urošević, D., Vucetić, M. M., Pavlović, M. Z., & Vukotić, B. 2013, *ApJ*, **777**, 31
- Baade, W., & Zwicky, F. 1934, *PNAS*, **20**, 259
- Badenes, C., Maoz, D., & Draine, B. T. 2010, *MNRAS*, **407**, 1301
- Baring, M. G., Ellison, D. C., & Jones, F. C. 1993, *ApJ*, **409**, 327
- Batejat, F., Conway, J. E., Hurley, R., et al. 2011, *ApJ*, **740**, 95
- Bell, A. R. 1978a, *MNRAS*, **182**, 147
- Bell, A. R. 1978b, *MNRAS*, **182**, 443
- Bell, A. R., Schure, K. M., & Reville, B. 2011, *MNRAS*, **418**, 1208
- Berezhko, E. G., & Völk, H. J. 2004, *A&A*, **427**, 525
- Berkhuijsen, E. M. 1987, *A&A*, **181**, 398
- Blair, W. P., Ghavamian, P., Sankrit, R., & Danforth, C. W. 2006, *ApJS*, **165**, 480
- Blandford, R. D., & Ostriker, J. P. 1978, *ApJL*, **221**, L29
- Bojičić, I. S., Filipović, M. D., Parker, Q. A., et al. 2007, *MNRAS*, **378**, 1237
- Borkowski, K. J., Hendrick, S. P., & Reynolds, S. P. 2007, *ApJL*, **671**, L45
- Borkowski, K. J., Hendrick, S. P., & Reynolds, S. P. 2006a, *ApJ*, **652**, 1259
- Borkowski, K. J., Williams, B. J., Reynolds, S. P., et al. 2006b, *ApJL*, **642**, L141
- Bozzetto, L. M., & Filipović, M. D. 2014, *Ap&SS*, **351**, 207
- Bozzetto, L. M., Filipović, M. D., Crawford, E. J., et al. 2010, *SerAJ*, **181**, 43
- Bozzetto, L. M., Filipovic, M. D., Crawford, E. J., et al. 2012a, *RMxAA*, **48**, 41
- Bozzetto, L. M., Filipović, M. D., Crawford, E. J., et al. 2012b, *MNRAS*, **420**, 2588
- Bozzetto, L. M., Filipović, M. D., Crawford, E. J., et al. 2013, *MNRAS*, **432**, 2177
- Bozzetto, L. M., Filipovic, M. D., Crawford, E. J., De Horta, A. Y., & Stupar, M. 2012c, *SerAJ*, **184**, 69
- Bozzetto, L. M., Filipovic, M. D., Haberl, F., et al. 2015, *PKAS*, **30**, 149
- Bozzetto, L. M., Filipovic, M. D., Urošević, D., & Crawford, E. J. 2012d, *SerAJ*, **185**, 25
- Bozzetto, L. M., Filipović, M. D., Urošević, D., Kothes, R., & Crawford, E. J. 2014a, *MNRAS*, **440**, 3220
- Bozzetto, L. M., Kavanagh, P. J., Maggi, P., et al. 2014b, *MNRAS*, **439**, 1110
- Brantseg, T., McEntaffer, R. L., Bozzetto, L. M., Filipovic, M., & Grieves, N. 2014, *ApJ*, **780**, 50
- Cajko, K. O., Crawford, E. J., & Filipovic, M. D. 2009, *SerAJ*, **179**, 55
- Callingham, J. R., Gaensler, B. M., Zanardo, G., et al. 2016, *MNRAS*, **462**, 290
- Chomiuk, L., & Wilcots, E. M. 2009, *AJ*, **137**, 3869
- Chu, Y.-H., & Kennicutt, R. C., Jr. 1988, *AJ*, **96**, 1874
- Chu, Y.-H., Kim, S., Points, S. D., Petre, R., & Snowden, S. L. 2000, *AJ*, **119**, 2242
- Clark, D. H., & Caswell, J. L. 1976, *MNRAS*, **174**, 267
- Crawford, E. J., Filipovic, M. D., de Horta, A. Y., Stootman, F. H., & Payne, J. L. 2008, *SerAJ*, **177**, 61
- Crawford, E. J., Filipović, M. D., Haberl, F., et al. 2010, *A&A*, **518**, A35
- Crawford, E. J., Filipović, M. D., McEntaffer, R. L., et al. 2014, *AJ*, **148**, 99
- Desai, K. M., Chu, Y.-H., Gruendl, R. A., et al. 2010, *AJ*, **140**, 584
- Davies, R. D., Elliott, K. H., & Meaburn, J. 1976, *MNRAS*, **81**, 89
- de Horta, A. Y., Filipović, M. D., Bozzetto, L. M., et al. 2012, *A&A*, **540**, A25
- de Horta, A. Y., Sommer, E. R., Filipović, M. D., et al. 2014, *AJ*, **147**, 162
- Dickel, J. R., Gruendl, R. A., McIntyre, V. J., & Amy, S. W. 2010, *AJ*, **140**, 1511
- Dopita, M. A., Blair, W. P., Long, K. S., et al. 2010, *ApJ*, **710**, 964
- Duric, N., & Seaquist, E. R. 1986, *ApJ*, **301**, 308
- Duric, N., Viallefond, F., Goss, W. M., & van der Hulst, J. M. 1993, *A&AS*, **99**, 217
- Efron, B., & Tibshirani, R. J. 1993, *An Introduction to the Bootstrap* (New York: Chapman Hall)
- Faraway, J. J., & Jhun, M. 1990, *J. Am. Stat. Assoc.*, **85**, 1119
- Feigelson, E., & Babu, G. 2012, *Modern Statistical Methods for Astronomy: With R Applications* (Cambridge: Cambridge Univ. Press)
- Fenech, D. M., Muxlow, T. W. B., Beswick, R. J., Pedlar, A., & Argo, M. K. 2008, *MNRAS*, **391**, 1384
- Ferrière, K. M. 2001, *RvMP*, **73**, 1031
- Filipović, M. D., & Bozzetto, L. M. 2016, arXiv:160401458F
- Filipović, M. D., Haberl, F., Winkler, P. F., et al. 2008, *A&A*, **485**, 63
- Filipovic, M. D., Haynes, R. F., White, G. L., & Jones, P. A. 1998, *A&AS*, **130**, 421
- Filipović, M. D., Jones, P. A., & Aschenbach, B. 2001, in *AIP Conf. Ser.* 565, *Young Supernova Remnants*, ed. S. S. Holt & U. Hwang (Melville, NY: AIP), 267
- Filipović, M. D., Payne, J. L., Reid, W., et al. 2005, *MNRAS*, **364**, 217
- Finke, J. D., & Dermer, C. D. 2012, *ApJ*, **751**, 65
- Gaensler, B. M., Haverkorn, M., Staveley-Smith, L., et al. 2005, *Sci*, **307**, 1610
- Galvin, T. J., & Filipovic, M. D. 2014, *SerAJ*, **189**, 15
- Galvin, T. J., Filipović, M. D., Crawford, E. J., et al. 2012, *Ap&SS*, **340**, 133
- Galvin, T. J., Filipović, M. D., Tothill, N. F. H., et al. 2014, *Ap&SS*, **353**, 603
- Gal-Yam, A., Mazzali, P., Ofek, E. O., et al. 2009, *Natur*, **462**, 624
- Ghavamian, P., Rakowski, C. E., Hughes, J. P., & Williams, T. B. 2003, *ApJ*, **590**, 833
- Glushak, A. P. 1985, *SvAL*, **11**, 350
- Glushak, A. P. 1996, *A&AT*, **11**, 317
- Gordon, S. M., Kirshner, R. P., Long, K. S., et al. 1998, *ApJS*, **117**, 89
- Green, D. A. 2005, *MmSAI*, **76**, 534
- Green, D. A. 2014, *BASI*, **42**, 47
- Grondin, M.-H., Sasaki, M., Haberl, F., et al. 2012, *A&A*, **539**, A15
- Haberl, F. 2014, in *Proc. ESA Conf., The X-Ray Universe*, ed. J.-U. Ness (Paris: ESA), 4
- Haberl, F., & Pietsch, W. 1999, *A&AS*, **139**, 277
- Haberl, F., Sturm, R., Ballet, J., et al. 2012, *A&A*, **545**, A128
- Harris, D. E. 1962, *ApJ*, **135**, 661
- Haynes, R. F., Klein, U., Wayte, S. R., et al. 1991, *A&A*, **252**, 475
- Hovey, L., Hughes, J. P., & Eriksen, K. 2015, *ApJ*, **809**, 119
- Hendrick, S. P., Borkowski, K. J., & Reynolds, S. P. 2003, *ApJ*, **593**, 370
- Hughes, A., Staveley-Smith, L., Kim, S., Wolleben, M., & Filipović, M. 2007, *MNRAS*, **382**, 543
- Hughes, J. P., Hayashi, I., Helfand, D., et al. 1995, *ApJL*, **444**, L81
- Hughes, J. P., Rafelski, M., Warren, J. S., et al. 2006, *ApJL*, **645**, L117
- Ingallinera, A., Trigilio, C., Umana, G., et al. 2014, *MNRAS*, **445**, 4507
- Jaskot, A. E., Strickland, D. K., Oey, M. S., Chu, Y.-H., & García-Segura, G. 2011, *ApJ*, **729**, 28
- Kavanagh, P. J., Sasaki, M., Bozzetto, L. M., et al. 2015a, *A&A*, **573**, A73
- Kavanagh, P. J., Sasaki, M., Bozzetto, L. M., et al. 2015b, *A&A*, **583**, A121
- Kavanagh, P. J., Sasaki, M., Bozzetto, L. M., et al. 2016, *A&A*, **586**, A4
- Kavanagh, P. J., Sasaki, M., Points, S. D., et al. 2013, *A&A*, **549**, A99
- Kavanagh, P. J., Sasaki, M., Whelan, E. T., et al. 2015c, *A&A*, **579**, A63
- Kiefer, J. 1953, *Proc. Am. Math. Soc.*, **4**, 502
- Kim, S., Staveley-Smith, L., Dopita, M. A., et al. 1998, *ApJ*, **503**, 674
- Kirk, J. G., & Heavens, A. F. 1989, *MNRAS*, **239**, 995
- Klein, U., Wielebinski, R., Haynes, R. F., & Malin, D. F. 1989, *A&A*, **211**, 280
- Klimek, M. D., Points, S. D., Smith, R. C., Shelton, R. L., & Williams, R. 2010, *ApJ*, **725**, 2281
- Kobayakawa, K., Honda, Y. S., & Samura, T. 2002, *PhRvD*, **66**, 083004
- Kostić, P., Vukotić, B., Urošević, D., Arbutina, B., & Prodanovic, T. 2016, *MNRAS*, **461**, 1421
- Krymskii, G. F. 1977, *SPhD*, **22**, 327
- Lakićević, M., van Loon, J. T., Meixner, M., et al. 2015, *ApJ*, **799**, 50
- Lee, J. H., & Lee, M. G. 2014, *ApJ*, **786**, 130
- Leonidaki, I., Boumis, P., & Zezas, A. 2013, *MNRAS*, **429**, 189
- Long, K. S., Blair, W. P., Kirshner, R. P., & Winkler, P. F. 1990, *ApJS*, **72**, 61
- Long, K. S., Blair, W. P., Winkler, P. F., et al. 2010, *ApJS*, **187**, 495
- Long, K. S., Helfand, D. J., & Grabelsky, D. A. 1981, *ApJ*, **248**, 925
- Lopez, L. A., Ramirez-Ruiz, E., Huppenkothen, D., Badenes, C., & Pooley, D. A. 2011, *ApJ*, **732**, 114

- Lukasiak, A., Ferrando, P., McDonald, F. B., & Webber, W. R. 1994, *ApJ*, **423**, 426
- Maggi, P., Haberl, F., Bozzetto, L. M., et al. 2012, *A&A*, **546**, A109
- Maggi, P., Haberl, F., Kavanagh, P. J., et al. 2014, *A&A*, **561**, A76
- Maggi, P., Haberl, F., Kavanagh, P. J., et al. 2016, *A&A*, **585**, A162
- Mathewson, D. S., & Clarke, J. N. 1973, *ApJ*, **180**, 725
- Mathewson, D. S., Ford, V. L., Dopita, M. A., et al. 1983, *ApJS*, **51**, 345
- Mathewson, D. S., Ford, V. L., Dopita, M. A., et al. 1984, *ApJS*, **55**, 189
- Mathewson, D. S., Ford, V. L., Tuohy, I. R., et al. 1985, *ApJS*, **58**, 197
- Mathewson, D. S., & Healey, J. R. 1964, in *IAU Symp. 20, The Galaxy and the Magellanic Clouds*, ed. F. J. Kerr (Cambridge: Cambridge Univ. Press), 283
- Meixner, M., Gordon, K. D., Indebetouw, R., et al. 2006, *AJ*, **132**, 2268
- Millar, W. C., White, G. L., Filipović, M. D., et al. 2011, *Ap&SS*, **332**, 221
- Mills, B. Y. 1983, in *IAU Symp. 101, Supernova Remnants and their X-ray Emission*, ed. J. Danziger & P. Gorenstein (Cambridge: Cambridge Univ. Press), 551
- Mills, B. Y., & Turtle, A. J. 1984, in *IAU Symp. 108, Structure and Evolution of the Magellanic Clouds*, ed. S. van den Bergh & K. S. D. de Boer (Cambridge: Cambridge Univ. Press), 283
- Mills, B. Y., Turtle, A. J., Little, A. G., & Durdin, J. M. 1984, *AuJPh*, **37**, 321
- Milne, D. K., Caswell, J. L., & Haynes, R. F. 1980, *MNRAS*, **191**, 469
- Ng, C.-Y., Zanardo, G., Potter, T. M., et al. 2013, *ApJ*, **777**, 131
- Ngishuchi, M., Yokogawa, J., Koyama, K., & Hughes, J. P. 2001, *PASJ*, **53**, 99
- O'Brien, A. N., Filipović, M. D., Crawford, E. J., et al. 2013, *Ap&SS*, **347**, 159
- Onić, D. 2013, *Ap&SS*, **346**, 3
- Ostrowski, M. 1991, *MNRAS*, **249**, 551
- Pacholczyk, A. G. 1970, *Radio Astrophysics. Nonthermal Processes in Galactic and Extragalactic Sources* (San Francisco, CA: Freeman)
- Pannuti, T. G., Duric, N., Lacey, C. K., et al. 2000, *ApJ*, **544**, 780
- Pannuti, T. G., Schlegel, E. M., Filipović, M. D., et al. 2011, *AJ*, **142**, 20
- Pannuti, T. G., Schlegel, E. M., & Lacey, C. K. 2007, *AJ*, **133**, 1361
- Park, S., Hughes, J. P., Slane, P. O., et al. 2003, *ApJL*, **592**, L41
- Park, S., Hughes, J. P., Slane, P. O., et al. 2012, *ApJ*, **748**, 117
- Pavlović, M. Z., Urošević, D., Vukotić, B., Arbutina, B., & Göker, Ü. D. 2013, *ApJS*, **204**, 4
- Payne, J. L., White, G. L., & Filipović, M. D. 2008, *MNRAS*, **383**, 1175
- Payne, J. L., White, G. L., Filipović, M. D., & Pannuti, T. G. 2007, *MNRAS*, **376**, 1793
- Pettitt, A. N. 1976, *Biometrika*, **63**, 161
- Pietrzyński, G., Graczyk, D., Gieren, W., et al. 2013, *Natur*, **495**, 76
- Reid, W. A., Stupar, M., Bozzetto, L. M., Parker, Q. A., & Filipović, M. D. 2015, *MNRAS*, **454**, 991
- Reynolds, S. P., & Chevalier, R. A. 1981, *ApJ*, **245**, 912
- Rosado, M., Laval, A., Le Coarer, E., et al. 1993, *A&A*, **272**, 541
- Sano, H., Yamane, Y., Voisin, F., et al. 2017, arXiv:170101962S
- Sasaki, M., Haberl, F., & Pietsch, W. 2000, *A&AS*, **143**, 391
- Seok, J. Y., Koo, B.-C., & Onaka, T. 2013, *ApJ*, **779**, 134
- Seward, F. D., Charles, P. A., Foster, D. L., et al. 2012, *ApJ*, **759**, 123
- Seward, F. D., Williams, R. M., Chu, Y.-H., et al. 2006, *ApJ*, **640**, 327
- Seward, F. D., Williams, R. M., Chu, Y.-H., Gruendl, R. A., & Dickel, J. R. 2010, *AJ*, **140**, 177
- Sheather, S. J. 2004, *StaSc*, **19**, 588
- Shklovskii, I. S. 1960, *SvA*, **4**, 243
- Silverman, B. 1986, *Density Estimation for Statistics and Data Analysis* (London: Taylor and Francis)
- Smith, C., Leiton, R., & Pizarro, S. 2000, in *ASP Conf. Ser. 221, Stars, Gas and Dust in Galaxies: Exploring the Links*, ed. D. Alloin, K. Olsen, & G. Galaz (San Francisco, CA: ASP), 83
- Smith, R. C., Kirshner, R. P., Blair, W. P., Long, K. S., & Winkler, P. F. 1993, *ApJ*, **407**, 564
- Spitzer, L. 1978, *Physical Processes in the Interstellar Medium* (New York: Wiley-Interscience)
- Staveley-Smith, L., Manchester, R. N., Gaensler, B. M., et al. 2005, in *IAU Coll. 192, Cosmic Explosions, On the 10th Anniversary of SN1993J*, ed. J.-M. Marcaide & K. W. Weiler (Cambridge: Cambridge Univ. Press), 89
- Stupar, M., Filipović, M. D., Jones, P. A., & Parker, Q. A. 2005, *AdSpR*, **35**, 1047
- Subramanian, S., & Subramaniam, A. 2010, *A&A*, **520**, A24
- Turtle, A. J., & Mills, B. Y. 1984, *PASAu*, **5**, 537
- Urošević, D. 2014, *Ap&SS*, **354**, 541
- Urošević, D., Pannuti, T. G., Duric, N., & Theodorou, A. 2005, *A&A*, **435**, 437
- Urošević, D., Vukotić, B., Arbutina, B., & Sarevska, M. 2010, *ApJ*, **719**, 950
- van den Bergh, S., & Tammann, G. A. 1991, *ARA&A*, **29**, 363
- Vukotić, B., Jurković, M., Urošević, D., & Arbutina, B. 2014, *MNRAS*, **440**, 2026
- Warren, J. S., Hughes, J. P., & Slane, P. O. 2003, *ApJ*, **583**, 260
- Warth, G., Sasaki, M., Kavanagh, P. J., et al. 2014, *A&A*, **567**, A136
- Wasserman, L. 2010, *All of Statistics: A Concise Course in Statistical Inference* (Berlin: Springer)
- Westerlund, B. E., & Mathewson, D. S. 1966, *MNRAS*, **131**, 371
- Williams, R. M., & Chu, Y.-H. 2005, *ApJ*, **635**, 1077
- Williams, R. M., Chu, Y.-H., Dickel, J. R., et al. 1999, *ApJS*, **123**, 467
- Williams, R. M., Chu, Y.-H., Dickel, J. R., et al. 2004, *ApJ*, **613**, 948
- Williams, R. M., Chu, Y.-H., Dickel, J. R., et al. 2005, *ApJ*, **628**, 704
- Williams, R. M., Chu, Y.-H., & Gruendl, R. 2006, *AJ*, **132**, 1877
- Woltjer, L. 1972, *ARA&A*, **10**, 129
- Zanardo, G., Staveley-Smith, L., Ball, L., et al. 2010, *ApJ*, **710**, 1515